

Role of pH and Eh in geothermal systems: Thermodynamic examples and impacts on scaling and corrosion

Samuel Bowman, Vikas Agrawal, Shikha Sharma *

Department of Geology and Geography, West Virginia University, 98 Beechurst Ave., Morgantown, WV 26506, USA

ARTICLE INFO

Keywords:

Geothermal Systems
pH
Eh
Scaling
Corrosion

ABSTRACT

The global demand for sustainable and clean renewable energy sources is rapidly increasing to meet growing energy demands while curtailing the CO₂ emissions from fossil fuels. Harnessing the natural heat or geothermal energy of the Earth's interior can simultaneously address both issues by offering a clean and renewable energy source. Enhanced geothermal systems require the movement and cycling of fluid through a porous rock media. This process requires understanding the chemistry occurring at the fluid-rock and fluid-metal interfaces both in the deep subsurface and surface, where fluid is circulated for energy transfer or storage. In this review paper, we evaluate the current state of research on how two key variables, pH and Eh, control the fluid-rock reactions controlling mineral scaling and the steel corrosion reactions associated with geothermal systems. These variables are frequently used in geochemical modeling to predict chemical reactions in geothermal systems. Prediction of the fluid-rock behavior can be utilized to formulate new strategies for extending the lifespan and efficiency of heat extraction and utilization and maximizing the safety of geothermal systems.

1. Introduction and background

While the use of the Earth's thermal energy has been exploited since antiquity, its first use as a source for the generation of electricity was conceived only recently in 1913 at Larderello, Italy (Fridleifsson, 2001; Cappetti and Ceppatelli, 2005; Fridleifsson et al., 2008; DiPippo, 2015). Despite the longstanding use of geothermal energy and the achievement at Larderello, it is instead, carbon-based fuels such as coal or oil dominate as energy sources (Fridleifsson, 2001; Suganthi and Samuel, 2012; Rodríguez et al., 2013; Hofmann et al., 2014; Anderson and Rezaie, 2019). Since electricity is one of the requisites for modern civilizations, and carbon fuels are well-established to be the primary cause of anthropogenic climate change via the release of greenhouse gasses-notably CO₂ (Ármansson and Kristmannsdóttir, 1992; Abas et al., 2017; Sharma et al., 2021), use of geothermal energy could prove worthwhile. Furthermore, as the world population is predicted to double by the end of the 21st century, the energy demand will increase dramatically (Fridleifsson, 2001; Gude, 2016). With global societal shifts in how electrical energy is derived coupled with the increasing demand for the quantity of energy itself, alternative energy sources have become more viable (Ármansson and Kristmannsdóttir, 1992; Fridleifsson, 2001; Suganthi and Samuel, 2012; Stutz et al., 2015;

Anderson and Rezaie, 2019). The advantages of geothermal energy are threefold, (1) it is a clean energy source (Tester et al., 1993; Fridleifsson, 2001, 2006; Fridleifsson et al., 2008; Majorowicz and Grasby, 2010; Bahadori et al., 2013; Rodríguez et al., 2013; Esteves et al., 2019), (2) it has the potential to generate tremendous quantities of energy (EPRI, 1978; Stefansson, 2005; Olasolo et al., 2016), and (3) it may be an additional method of water desalination (Tester et al., 1993; Gude, 2015, 2016).

An enhanced geothermal system (EGS) utilizes the Earth's natural geothermal gradient to generate energy either as electricity or heat. The heat is generated from either radioactive decay (Bahadori et al., 2013) or from the heat retained since the planet's formation (Ghosh, 2011). An EGS is a human-altered (enhanced) hydrothermal system. Indeed, Ellis (1979) discusses the importance of studying and conducting experiments using geothermal systems to elucidate problems encountered in hydrothermal ore deposit research. Hot dry rock(s) (HDR) are those whose low permeability prevents the passive flow of pore fluids (Mock et al., 1997; Carlin, 2004). Conceptually, an EGS functions by the recirculation of fluid from the surface (injection well) to a subsurface reservoir (Fig. 1) (Ghosh, 2011; Kazemi and Samadi, 2016; Wu and Li, 2020). In the case of a commercial EGS designed for generating and distributing electricity, the hot fluid is returned to the surface

* Corresponding author.

E-mail address: shikha.sharma@mail.wvu.edu (S. Sharma).

(production well), where its thermal energy is converted into electrical energy using a steam-operated turbine (van der Meer et al., 2014; DiPippo, 2015). By default, these systems require a fluid temperature sufficient to boil water and are typically over 150 °C (Mock et al., 1997; Bai et al., 2012). However, electricity can be produced from 100 °C water (e.g., Majorowicz and Weides, 2012 and references therein). If the temperature of the geothermal fluid is lower than the boiling point of water (<100 °C), or in the absence of ORC, geothermal energy may still be utilized for direct heating (i.e., residential homes) (Lund, 1997; Mock et al., 1997; Páztay et al., 1998; Ghosh, 2011; Bai et al., 2012; Hofmann et al., 2014). Deep Direct Use (DDU) is a specific form of direct-use heating applied to EGS reservoirs typically greater than 2 km in depth (e.g., Beckers et al., 2021).

EGS improves the initial HDR permeability by utilizing a hydraulic fracturing technique (Mock et al., 1997; von Jouanne and Brekken, 2017; Esteves et al., 2019). Increasing the permeability of the subsurface reservoir is essential as it leads to higher fluid mass flow rates (Tester et al., 2006), thereby increasing the heat delivered to the production well. The fracture networks play a crucial role in carrying the fluids from the injection well to the recovery well and directly control the heat transfer rate and the rate at which energy can be extracted from the

geothermal reservoir. The fluid-rock interactions in the geothermal reservoir play a key role in controlling fracture transmissivity via dissolution, precipitation, and scaling reactions. These reactions have a direct impact on the reservoir performance and longevity.

Therefore, it becomes critically important to understand and predict the fluid-rock interaction occurring within the reservoir after the fluid is introduced in geothermal reservoirs having different depths, mineralogies, and fluid chemistries. Predicting reactions and chemical relationships within the EGS reservoir can increase its lifespan and reduce the associated with developing an EGS site (Tester et al., 2006). Besides, the loss of transmissivity of fracture networks in the reservoir, scaling, and corrosion in the wellbore, and water delivery pipelines on the surface can also severely hinder the efficiency of the geothermal system (Nogara and Zarrouk, 2018a, 2018b; Li et al., 2020; Zolfagharroshan and Khamehchi, 2020; Bu et al., 2022). This review paper discusses the current understanding of how two key geochemical variables, pH and Eh, control the fluid-rock reactions in the reservoir, corrosion reactions, mineral dissolution, and mineral scaling in geothermal systems. We also provide recommendations on how to prevent scaling and corrosion in geothermal systems and suggestions for future research directions.

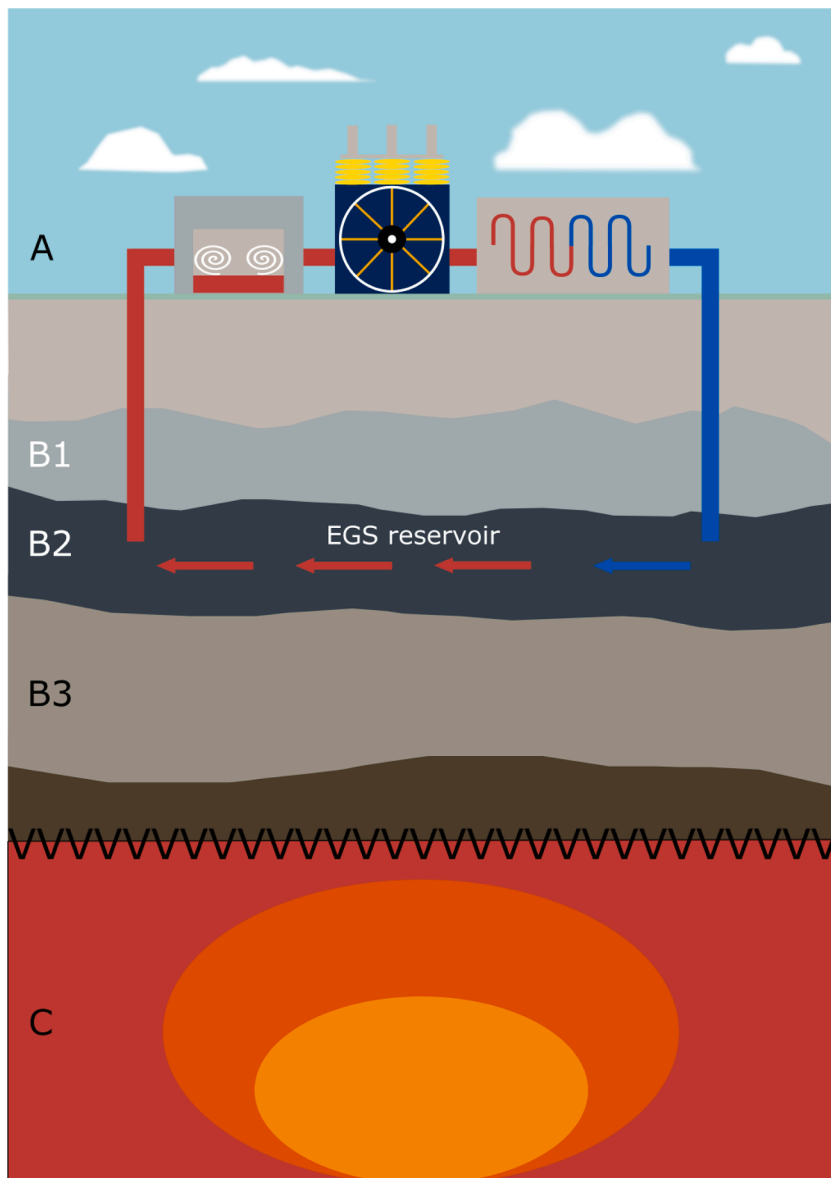


Fig. 1. Cartoon illustrating a simplified geothermal system (not to scale). (A) At the surface, an electrical power plant contains an injection well (right side, blue arrow) that pumps the working fluid (typically water) into the EGS reservoir (B2). The working fluid is vertically constrained within the reservoir by overlying (B1) and underlying (B3) rocks. Thermal energy from the mantle (C) sufficiently warms overlying HDR units. The hot fluid in the EGS reservoir (left side, red arrow) then travels back to the surface where steam powers a turbine and is transferred to the electrical grid. The geothermal water has now lost considerable heat and the cycle repeats as it is once again pumped into the EGS reservoir.

2. Master variables in geochemical reactions in geothermal systems

While many variables are involved in geochemical reactions in geothermal systems, some are fundamental and impart more control than others. Compiling and reviewing these master variables can assist with predicting the possible geochemical outcomes occurring both at reservoir conditions and on the surface (production side). Moreover, even if the exact outcome cannot be determined, the number of outcomes may be reduced, constraining an otherwise unwieldy system. The fundamental variables explored herein are pH and Eh (which themselves are directly related to temperature and pressure), which are first outlined theoretically before their interplay with critically important topics including ionic strength (I.S.), kinetics (as dissolution), speciation, corrosion, and scaling (as precipitation).

The reviewed literature and presented analysis examine pH and Eh only in an inorganic context. Exploring these variables discretely is difficult as they are closely linked and interrelated. For example, it is impossible to explain mineral solubility in terms of temperature alone, as the ionic activity in the fluid is linked to the dissolution of the reservoir rocks—which is controlled by pH. Nonetheless, these variables are put forth separately in hopes of outlining how they control the chemistry of fluid-rock interaction in EGS.

2.1. pH

Aqueous fluids are most often described in terms of pH. However, it is worth noting that aqueous fluids could be described in terms of pOH since the dissociation of pure water slightly produces not only acid (H^+) but base (OH^-) as well, having an equilibrium value of 10^{-14} (e.g., Fitts, 2002). The equilibrium value indicates that pure water will dissociate into equal concentrations of acid [H^+] and base [OH^-], although equilibrium is temperature-dependent. However, the pH is not static in natural systems such as geothermal environments (unless a steady-state is reached) because of exchange occurring at the water-rock interface where H^+ and OH^- are released or consumed.

Water in equilibrium with the atmosphere is naturally acidic to the partitioning of gaseous CO_2 into the liquid solution, thereby producing carbonic acid (H_2CO_3), as



(Fetter, 2001; Fitts, 2002). The classic Bjerrum plot illustrates the effect of pH on phase speciation in the CO_2 – HCO_3^- – CO_3^{2-} system. In the carbonate-dominant pH region, calcite will precipitate if [CO_3^{2-}] and [Ca^{2+}] are sufficiently high. Precipitation will consume alkalinity and reduce buffering capacity and lower the pH. The concentration of [H^+] may drive a reaction towards dissolution or precipitation. Calcite solubility increases in the presence of CO_2 (García et al., 2006), while precipitation is favored at high pH. Conversely, the solubility of amorphous silica is inversely proportional to [H^+], and precipitation is favored at low pH (more soluble at high pH), while quartz solubility is indifferent at $pH < 8$ (Corsi, 1986).

As both pH and total ion concentration are important factors in predicting fluid behavior in subsurface reservoirs (Garrido Schneider et al., 2016; Loredó et al., 2017; Varga et al., 2019), and surface operations involving natural waters (e.g., Rafferty, 1999; Antony et al., 2011), it becomes necessary to model the solution with respect to these variables. Moreover, for minerals that dissolve at low pH, the total dissolved solids (TDS) in the solution will increase. The concentration (thus TDS) can still change at constant temperature and pH due to the water-rock ratios (Seyfried and Mottl, 1982). Data presented by these workers indicates an inverse relationship between the water-rock ratio and the concentration of Al, Ba, K, Mn, Si, Sr, and Zn in solution (higher concentrations result from lower water-rock ratios). Additionally, the mixing of relatively dilute meteoric water with water of much higher

TDS such as saline water or marine water, may shift mineral scaling from undersaturated to supersaturated (Arnórrsson, 1992). The saturation index (Ω) or (SI) is defined as the ratio of the ion activity product (IAP) to the fluid solubility (K_{sp}) and is given as

$$SI = \Omega = \frac{IAP}{K_{sp}} \quad (2)$$

$SI < 1$ indicates undersaturation, $SI = 1$ indicates saturation (at equilibrium), and $SI > 1$ indicates supersaturation (e.g. Andrews et al., 2004; Chen et al., 2016; Crundwell, 2017; Sim et al., 2018). Some workers report SI instead as a $\log(IAP/K_{sp})$ where 0 indicates saturation (e.g., Criaud et al., 1989; Shaver, 1993; Simmons and Christenson, 1994; Ungemach 2003; Chidambaram et al., 2011). Additionally, some workers write SI as $\log(Q/K)$, replacing IAP for Q (Arnórrsson, 1992; Spycher and Reed 1992). In whichever case, the IAP is calculated by multiplying the activities of the ions produced in the forward direction of an equilibrium reaction (Eq. (3)). A generalized mineral equilibrium reaction is



An activity is computed for both a^+ cations and b^- anions by converting the measured concentration [x_i] in molarity to activity [a_i] also in molarity, by an activity coefficient γ_i , where

$$[a_i] = \gamma_i[x_i] \quad (4)$$

The γ_i for each species may be calculated according to various models using Eqs. (7)–(9), and (12) below, but first, the I.S. is determined for the solution. This term differs from total dissolved solids (TDS) as it considers both the concentration and charge of each dissolved species. I.S. is summed for every i th species in solution using the charge of each species (z_i) and is given as

$$I.S. = \frac{1}{2} \sum [x_i]z_i^2 \quad (5)$$

Note that the charge of the species is squared, indicating that some species will contribute more to the I.S. than others at the same concentration (e.g. PO_4^{3-} versus Br^-). Both [H^+] and [OH^-] are present in geothermal fluids; their abundance (thus pH, or pOH) directly affects I.S., activity, and, ultimately mineral solubility (K_{sp}). It is important to note that solutions are electrically neutral (McQuarrie and Simon, 1997) and that

$$\sum_{anion} [x_i]z_i^2 + \sum_{cations} [x_i]z_i^2 = 0 \quad (6)$$

In the case of an outstanding net positive charge balance, Cl^- should be used to compensate for the lack of anions because its effect on pH is negligible (Marion, 2001). The outstanding positive charge has been accommodated by balancing with HCO_3^- alone (Dobson et al., 2021)—however, increasing the concentration of HCO_3^- or CO_3^{2-} may result in significant changes to pH and is not advised (Marion, 2001). Finally, the concentration units above are in molarity (mol/L solvent), although in high temperature and pressure geothermal environments, it should be given in molality instead (mol/kg solvent). Mass/mass units are preferred since geothermal waters often have high temperatures which cause the water volume to change, affecting density. For example, mass-normalized water at a high temperature will have a lower density than the same water at a low temperature. Molality requires that the water or solvent density be known. If this value is unknown, Monnin (1994) provided a computer program for the density calculation of natural water.

At low I.S. activities are similar or equal to concentration ($\gamma_i = 1$). However, geothermal fluids may contain very high TDS, leading to high I.S. (Miller, 1980)—particularly in sedimentary facies (Ungemach, 2003). Examples include TDS $> 250,000$ mg/L in the Salton Sea Geothermal System (Williams and McKibben, 1989), up to 265,000 mg/L at the Groß Schönebeck geothermal site (Regenspurg et al., 2010). Groundwaters may have TDS up to $\sim 400,000$ mg/L in the Appalachian Basin (Rowan

et al., 2011) and even above 600,000 mg/L in the Michigan Basin (Wilson and Long, 1993). Fluid inclusion data has shown that the salinity of hydrothermal fluids may range from ~0 to >40 wt% (Roedder, 1979). In either case, the concentration and activities will be highly dissimilar because $\gamma \ll 1$. Geothermal fluids often possess high I.S., indicating they are well-suited to activity modeling (Miller, 1980). Three activity coefficient models are given below; the Debye-Hückel Model (Eq. (7)), Debye-Hückel-Extended Model (Eq. (8)), and the Davies Model (Eq. (9)). In order, these are as follows;

$$\gamma = 10^{\log\gamma} = \log\gamma = -Az_i^2\sqrt{I}, \text{ and} \quad (7)$$

$$\gamma = 10^{\log\gamma} = \log\gamma = \frac{-Az_i^2\sqrt{I}}{1 + Ba_o\sqrt{I}}, \text{ and} \quad (8)$$

$$\gamma = 10^{\log\gamma} = \log\gamma = \frac{-Az_i^2\sqrt{I}}{1 + \sqrt{I}} + 0.3I. \quad (9)$$

Where a_o is the ionic diameter in Angstroms for the relevant atom or molecule (e.g., Slater (1964) and for polyatomic radii; Jenkins and Thakur (1979)). Note that I in Eqs. (7)–(9) and (12) is ionic strength (I. S.). While values for the coefficients A and B are known up to 100 °C (373.15 K), the temperature(s) of geothermal fluids are often greater. It is risky to assume that the same linear behavior of A and B will continue at temperatures beyond the boiling point of water, and extrapolation is not recommended. However, for $T < 100$ °C, A and B values may be interpolated from Eqs. (10) and (11), respectively, which are lines of best fit from the data in Manov et al. (1943). For A;

$$A(T) \approx 1.003 * 10^{-3}(K) + 0.2003, \text{ and} \quad (10)$$

$$B(T) \approx 1.653 * 10^{-4}(K) + 0.2788, \text{ for B.} \quad (11)$$

Despite this limited temperature range, $T < 100$ °C are relevant to direct-use geothermal operations (Bloomquist, 2003) and similar to reinjection temperatures (Kamila et al., 2021). For very high I.S. values (up to 6 M), the Pitzer equations (Pitzer, 1973; Pitzer and Mayorga, 1973) best determine γ . These equations are extensive and numerous; however, their computation may be performed by the computer software PHRQPITZ (Plummer et al., 1988) within PHREEQC v3 (Parkhurst and Appelo, 2013). Additionally, the Bromley activity model can be used for I.S. up to 6 M (Bromley, 1973) and is much simpler to calculate, as

$$\gamma = 10^{\log\gamma} = \log\gamma = \frac{-A\gamma_{abs}(Z_+Z_-)\sqrt{I}}{1 + \rho\sqrt{I}} + \frac{(0.06 + 0.6B)abs(Z_+Z_-)I}{\left(1 + \frac{1.5}{abs(Z_+Z_-)}I\right)^2} + BI. \quad (12)$$

This activity model uses the same A value in Eqs. (7)–(9). Z_+ and Z_- correspond to the charges of the cation and anion salt pair, respectively. Values of ρ are frequently taken as unity, although for some salts (1–3 (e.g., K_3PO_4) and 3–1 (e.g., $AlCl_3$) salts have ρ of 1.4, while 4–1 salts have ρ of 1.6, and B is a characteristic value for the salt (Bromley, 1973). This worker notes that B values are temperature-dependent and are adjusted using additional values (B_1, B_2, B_3). Unfortunately, these values may not be available for the desired salt.

2.1.1. pH and dissolution kinetics

Determining the reaction direction (precipitation or dissolution) for a water-rock interaction is useful, but must be considered alongside the reaction rate. If a geothermal fluid is undersaturated (depleted in ion activity) with respect to the components of a solid mineral, then the fluid is in disequilibrium, allowing for the dissolution of the mineral. However, the rate of this reaction may be sufficiently low such that very little solid mineral enters the aqueous phase (slight change in IAP with respect to the components of that mineral). The relationship between pH and the rate of a reaction is well documented by the following modified

expression (from; Hellmann, 1994; Lasaga et al., 1994; Ganor et al., 1995)

$$k \propto a_{H^+}^n. \quad (13)$$

The exponent n is a number $-1 < n < 1$, indicating that the reaction rate (k) may either increase or decrease and is simply the slope of $\log k$ (mole/m²s) (y) versus $\log k$ (mole/m²s) (x) (Hellmann, 1994; Ganor et al., 1995). The value of n is mineral and pH domain (mechanism)-specific (Furrer and Stumm, 1986). Since a reaction may occur over many pH orders, there are three pH domains or mechanisms that each have their own n and k . The three pH ranges are broadly ascribed for the mineral albite by Hellmann (1994) to be: acid, $pH \leq 5$, neutral $pH 5$ to 8.6, and base $pH \geq 8.6$, and for muscovite by Lammers et al. (2017) to be: acid $pH 2$ to 2.6, neutral $pH 5.6$ –7.2, and base $pH 7.4$ to 9.5. Values of both n and k for each mechanism may be found in tables such as in Palandri and Kharaka (2004), who also provide a full kinetic equation for all three mechanisms for $T \neq 298.15$ K, as

$$r = \frac{dm}{dt} = -A \left(\left(k_{acid298.15} \kappa \exp\left(\frac{-E_{acid}}{R} \left(\frac{1}{T} - \frac{1}{298.15 K}\right)\right) a_{H^+}^{n_{acid}} \right) (1 - \Omega^p)^q \right) + \left(k_{neutral298.15} \kappa \exp\left(\frac{-E_{neutral}}{R} \left(\frac{1}{T} - \frac{1}{298.15 K}\right)\right) \right) (1 - \Omega^p)^q + \left(k_{base298.15} \kappa \exp\left(\frac{-E_{base}}{R} \left(\frac{1}{T} - \frac{1}{298.15 K}\right)\right) a_{H^+}^{n_{base}} \right) (1 - \Omega^p)^q \right). \quad (14)$$

Lasaga et al. (1994) note that a full, triple-mechanism kinetic rate equation is preferable to a single-mechanism kinetic rate equation (e.g., Giggenbach (1984)). Often dm/dt is written as R , but we opt for r to avoid confusion with the gas constant R (0.001987 kcal/Kmol, or 0.008314 kJ/Kmol). The $(1 - \Omega^p)^q$ term considers the decrease in r as the dissolution reaction approaches equilibrium (Lasaga et al., 1994; Lammers et al., 2017), at which $r = 0$. The values of p and q are empirically determined and thus are taken as unity unless otherwise known (Palandri and Kharaka, 2004). As above, the kinetics of fluid-rock interactions are directly related to the ion activity of the solution. Indeed as r is a measure of dissolved ion abundance over time, indicating kinetics is inseparable from ion activity. For a constant surface area with a fluid near equilibrium ($\Omega \approx 1$) and $p = q = 1$, Eq. (14) simplifies to

$$r = \frac{dm}{dt} = \left(\left(k_{acid298.15} \kappa \exp\left(\frac{-E_{acid}}{R} \left(\frac{1}{T} - \frac{1}{298.15 K}\right)\right) a_{H^+}^{n_{acid}} \right) \right) + \left(k_{neutral298.15} \kappa \exp\left(\frac{-E_{neutral}}{R} \left(\frac{1}{T} - \frac{1}{298.15 K}\right)\right) \right) + \left(k_{base298.15} \kappa \exp\left(\frac{-E_{base}}{R} \left(\frac{1}{T} - \frac{1}{298.15 K}\right)\right) a_{H^+}^{n_{base}} \right) \right) \quad (15)$$

2.2. Eh

Prediction of chemical reactions and the potential for future reactions is helpful in understanding the fluid-rock interaction of an EGS. The behavior of two or more chemical species can be determined according to the Gibbs free energy of the (possible) reaction. If the speciation of the reactant and geothermal fluid parameters are known, then the speciation of the product resulting from a chemical reaction may be determined. Such speciation of products or reactants is primarily determined (along with pH) by the amount of free O_2 or redox potential (Eh). For instance, in the oxygen-hydrogen-sulfur system, the crystalline product of a reaction may be sulfur (S^0), gypsum ($CaSO_4 \cdot 2H_2O$, in the presence of Ca^{2+}), or pyrite (FeS_2 in the presence of iron). Whichever mineral phase is present and is available for participation in chemical reactions depends upon the speciation of the components, both cation and anion. While pH measures the activity of H^+ in solution, Eh is measured in volts and therefore is effectively the electron activity (Fetter, 2001). Oxidation reactions involve the transfer of electrons from reactants to products. For example, reduced sulfur in sulfide (as S^{2-})

loses eight electrons and undergoes a speciation change to oxidized sulfur in sulfate (as S^{6+}), where



The oxidation occurs when the reduced sulfur is exposed to an electron acceptor such as O_2 . Due to the production of available sulfate, the fluid may become supersaturated, resulting in the precipitation of sulfate minerals. These types of reactions also release acid, which is closely linked with oxidation as

$$Eh \propto \frac{1}{pH} \quad (17)$$

Bass-Becking et al. (1960) make a similar observation in that Eh and pH are effectively the measures of $[e^-]$ and $[H^+]$ where the release of one comes at the expense of the other.

Typically, the amount of free O_2 available in geothermal systems is minimal (Miller, 1980; Giggenbach, 1987). There is a strong vertical or depth component to redox buffering (controlled by plagioclase-clay boundary) along the meteoric (reduced)-magmatic (oxidized) interface (Giggenbach, 1977, 1981). Natural waters in equilibrium with the atmosphere will have oxidizing Eh values due to the abundant O_2 . At a pH of 0, the most oxidized water has an Eh value of ~ 1.2 V (Eq. (20)). Similarly, the Eh values of near-surface waters with a typical pH ranging from 4 to 9 (Fetter, 2001) corresponds to ~ 1 V and ~ 0.7 V respectively (also using Eq. (20)). The stability of liquid water occupies the domain between H_2 and O_2 (Fig. 2). The redox potential between oxidized O_2 and reduced H_2 and thus the stability field of liquid water is separated by ~ 1.23 V, a value that holds across the pH scale. Bass-Becking et al. (1960) report compiled Eh values of geothermal waters ranging from ~ -0.3 V to $\sim +0.7$ V. These data are predominately from Rotorua, New Zealand, and Fergusson Island, New Guinea, both high-temperature geothermal systems Lahan et al. (2020), and Giggenbach and Glover (1992) respectively. Low-temperature geothermal systems common in

sedimentary basins have yielded similar, perhaps less oxidizing Eh values overall. Moreover, the lack of measurable O_2 provides a priori evidence of reducing conditions (Criaud et al., 1989). Due to the low availability of O_2 at low temperatures (< 500 °C), the redox potential can still be obtained using $R_H \approx \log(x_{H_2}/x_{H_2O})$ instead (Giggenbach, 1987)-smaller R_H indicates greater oxidation potential. This further supports the reduced redox characteristic of geothermal fluids compared to hotter, more oxidized magmatic fluids (e.g., Giggenbach, 1981). Andrews and Kay (1983) report reducing Eh values of -0.3 V in the Wessex Basin sedimentary basin groundwaters at depths up to ~ 1.75 km and oxidizing values up to $+0.3$ V (unfortunately, depths are not provided; therefore, it is assumed these waters are close to the surface). Similar values from the Paris Basin range from -0.35 to -0.15 V at $1600 \leq m \leq 2000$ depth and temperatures < 85 °C (Criaud et al., 1989). For the volcanic-low-temperature hybrid-type system at Paratunka, Eh values range from -0.18 to -0.15 V (Bragin et al., 2018). The Paratunka site, despite being hosted in volcanic facies, has a redox potential more similar to what would be found in sedimentary facies. The altered sediments of the Salton Sea Geothermal Field (Younker et al., 1982) have an Eh of -0.22 V (Gallup et al., 1995). It is important to note that as reservoir fluid returns to the surface, not only will the pressure reduce due to degassing, but it will be exposed to significantly greater amounts of O_2 (an oxidant). Exposure to atmospheric oxygen will substantially affect the redox state of components in the fluid. Finally, in high temperature and pressure metamorphic settings, H_2 (a reductant) is produced by water-rock (FeO mineral) interaction during serpentinization (McCollom and Bach, 2009). Mineralogical evidence of this low Eh regime can be confirmed by the presence of certain diagnostic Fe-Ni minerals such as heazlewoodite (Ni_3S_2) (Frost, 1985; Alt and Shanks, 1998) or awaruite ($FeNi_3$) (Alt and Shanks, 1998). A natural geothermal area where these minerals may be found is along the Highland Group-Vijayan Complex boundary in Sri Lanka (Dissanayake and Jayasena, 1988).

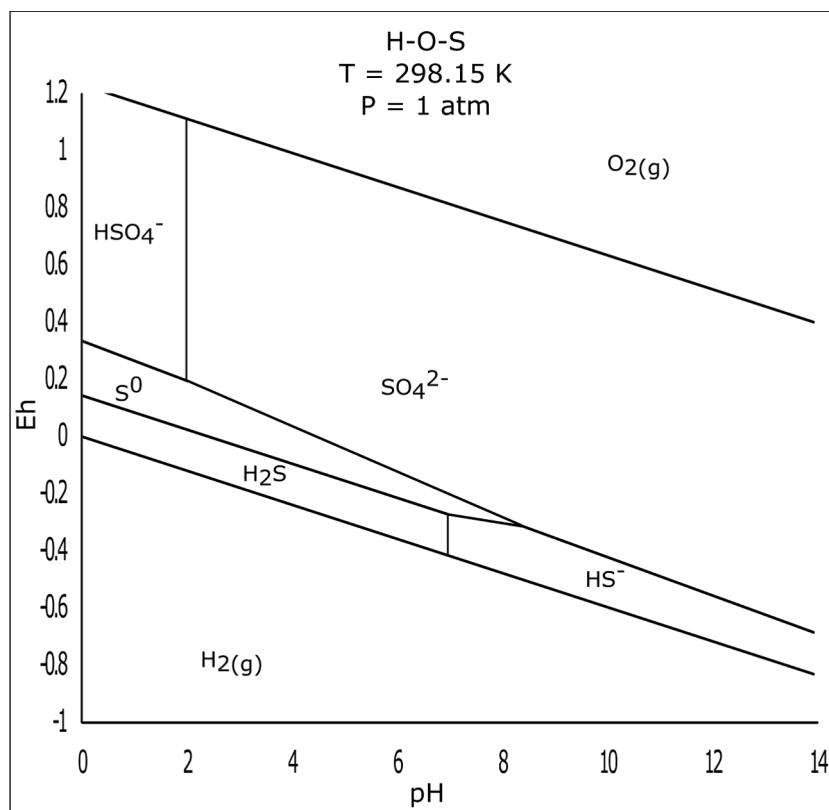


Fig. 2. H—O—S system at 25 °C and 1 atm found using the IGL at fixed ionic strength. The area between the O_2 and H_2 lines denotes the stability field of H_2O . 1 atm is 0.101325 MPa at 298.15 K. The pressure contours are determined using μ_p and μ_o determined from IGL volumes.

3. Influence of pH and Eh on fluid-rock interaction

3.1. Phase speciation

Obtaining accurate Eh data from a fluid is problematic because the fluid may be in electric disequilibrium (Hem, 1960; Criaud et al., 1989; Stefánsson and Arnórsson, 2002), resulting in apparent values. This is because the Eh, or redox state of the fluid is sometimes affected by kinetics (Pourbaix, 1974). Additionally, Eh values are often varied within a sample (Criaud et al., 1989; Scheiber et al., 2012), further increasing the difficulty in interpretation. Even still, speciation can be presented graphically using a Pourbaix (or Eh-pH) diagram (Pourbaix, 1949). Isoleths along the diagram indicate both stability regions for specific species in the fluid as well as lines of equilibrium between adjacent species. Such diagrams have become ubiquitous in fluid-rock geochemical literature and useful for modeling geothermal systems. An Eh-pH diagram is an activity-activity diagram of a multi-component system with stability fields of relevant species. While these diagrams are helpful, it is essential to remember that there could be more than one species present at a given (pH, Eh) coordinate and that a specific stability field merely indicates the dominance of that particular species (Rojas-Hernández et al., 1991). Additionally, stability fields are subject to the pH of the solution. For example, as might be expected, and in accordance with a Bjerrum plot, the Eh-pH stability field between UO_2^{2+} - UO_2CO_3^0 shifts to the left (lower pH) due to an increase in pCO_2 (Andrews and Kay, 1983). Finally, the redox state is subject to the pair chosen (e.g., SO_4^{2-} - S^{2-} or Fe^{2+} - Fe^{3+}), and the same fluid composed of multiple redox pairs will yield different potentials (Nordstrom and Munoz, 1994). This suggests that multiple redox pairs should be considered to improve confidence in the complete redox potential of the water in question. The measured redox potential is a bulk measurement of all redox pairs in the solution.

A brief outline for the construction of Eh-pH diagrams is given here but is not intended to be exhaustive. Numerous thorough examples provide much greater detail (Williams and Patrick, 1977; Huang and Cuentas, 1989; Rojas-Hernández et al., 1991; Verink, 2000), but we found that of Hem (1960) to be the most straightforward. There are three types of isopleth contour lines in Eh-pH diagrams; vertical (pH), horizontal (Eh), and sloped (Eh is a function of pH). Following Hem (1960), these are given in such order as;

$$\text{pH} = -\frac{1}{h} \left(\frac{\Delta G_r}{RT\lambda} \right) + \log \left(\frac{a_p^r}{a_p^r} \right), \quad (18)$$

$$\text{Eh} = \frac{\Delta G_r}{nF} - \left(\frac{RT\lambda}{n} \right) \log \left(\frac{a_p^r}{a_p^r} \right), \text{ and} \quad (19)$$

$$\text{Eh}(\text{pH}) = - \left(\frac{RT\lambda}{n} \right) h + E^\circ. \quad (20)$$

Where h is the stoichiometric value for H^+ in a reversible reaction (e.g., $h = 9$ in Eq. (15)), the Gibbs free energy of the reaction is denoted as ΔG_r (more detail in Section 3.2.3), and the RT/F term is often written as V_T whose terms are the gas constant, temperature and the Faraday constant (96,485 C/mol) respectively. The value of λ is 2.3026, and n is the number of free electrons (e.g. $n = 8$ in Eq. (16)). The exponent of the activities of the product (a_p) and reactant (a_r) are their respective stoichiometric coefficient (e.g., $r = 4$ as $4\text{H}_2\text{O}$ in Eq. (16)). Note that equilibrium, the activities of a_p and a_r are the same, although their exponents may differ. E° is the intercept of sloped lines and may be found in thermodynamic tables (e.g., CRC). E° is the equilibrium potential and may be calculated by the first term in Eq. (19) ($E^\circ = \Delta G_r/nF$). For the sloped line in Eq. (20), the negative slope affirms the inverse relationship (from Eq. (17)) between pH and Eh. This relationship is observed in

other multi-component systems (e.g., Pourbaix, 1949; Williams and Patrick, 1977; Huang, and Cuentas, 1989; Huang 2016).

As calcite was used in the previous section, the oxygen-hydrogen-sulfur system will be explored below in relation to Eh. Hydrogen sulfide (H_2S) is a common gas in geothermal systems (Henley and Brown, 1985; Finster et al., 2015), and sulfate (SO_4^{2-}) is one of the most common anions in hydrothermal fluids (Roedder, 1979). While we do not include a metal(oid) cation in the example given below, sulfide minerals commonly form undesired scales in EGS operations (Phillips et al., 1977; Criaud and Fouillac, 1989; Brown, 2011). Fig. 2 displays the Eh-pH stability fields for common species in the H—O—S system at STP conditions. Liquid water is stable above the H_2 (H_2S , HS^-) equilibrium contour line and below the O_2 (SO_4^{2-} , HSO_4^-) equilibrium contour lines. The H_2 stability field is the most reducing region of the diagram and is associated with Eh values < 0 V. Conversely, the oxidizing region of the diagram has high Eh values and is oxygen-rich. With respect to liquid water, reducing waters are those where sulfides (HS^- or H_2S) are present, while oxidizing waters are those where sulfates (HSO_4^- or SO_4^{2-}) are present (Brookins, 1988). Note the elemental sulfur (S^0) stability field. Since this species is solid, it would precipitate out of the fluid and lead to scaling in the geothermal system (Section 4.2). The SO_4^{2-} ion occupies the greatest stability area in the H—O—S system at this Eh range. It shares the most equilibrium contour boundaries and can react with free electrons (moving vertically) or acid (moving horizontally) to form any species in the H—O—S diagram except for H_2S or H_2 . When SO_4^{2-} is a product in an equilibrium reaction with its neighboring species, the Gibbs free energy (more in Section 3.2.3) is positive. This indicates that SO_4^{2-} is an unfavorable product in the pH-Eh space presented in Fig. 2. While SO_4^{2-} may not be thermodynamically preferred, it does not mean that transition to the preferred sulfur speciation is an immediate process. As mentioned in Section 3.1, redox disequilibrium is expected and can be confirmed by mineral-fluid assemblages (e.g., O_2 and reduced iron simultaneously present) (Nordstrom and Munoz, 1994). Interestingly, sulfate expressed as a solid, as in gypsum ($\text{CaSO}_4 \cdot 2\text{H}_2\text{O}$) or anhydrite (CaSO_4) is noted for its inert behavior (Machel, 2001).

3.2. Phase speciation in non-standard temperature and pressure

3.2.3. Eh-pH stability fields at non-standard temperature

The example provided in Eq. (16) is written as an equilibrium reaction and could therefore proceed in either the forward or reverse direction (provided there is enough energy available for the non-spontaneous reaction direction). The amount of energy (if required) and the favorability of a reaction are provided by obtaining the Gibbs free energy of the reaction (ΔG_r), defined as

$$\Delta G_r^\circ = \Delta G_p^\circ - \Delta G_r^\circ = (\Delta H^\circ - T\Delta S^\circ)_p - (\Delta H^\circ - T\Delta S^\circ)_r \quad (21)$$

where T is in Kelvin, ΔH and ΔS are the enthalpy and entropy of reaction at STP, respectively. These values are available in tables and pertain to the components of a reaction (i.e., HS^- , H_2O , and SO_4^{2-}).

Since geothermal fluids are present at temperatures much greater than 25°C , ΔG_T is then the Gibbs free energy at some $T \neq 298.15$ K, and is;

$$\Delta G_T = (\Delta H^\circ - T_T\Delta S^\circ)_p - (\Delta H^\circ - T_T\Delta S^\circ)_r. \quad (22)$$

Fig. 3 compares the stability fields from Fig. 2 to elevated temperatures of 100°C (for a low-temperature geothermal system) and 200°C (for a high-temperature geothermal system). At a pressure of 1 atm, this figure approximates the Eh-pH relationships of a geothermal fluid at the surface (i.e., geothermal fluid in a power plant or direct-use grid system). Note that Figs. 3 and 4 represent general trends because (for simplicity) heat capacity was not considered, but acknowledge that including it would yield more accurate speciation diagrams. In the H—O—S system, an increase in temperature tends to drive the Eh of the fluid to more reducing conditions. This observation is in agreement with

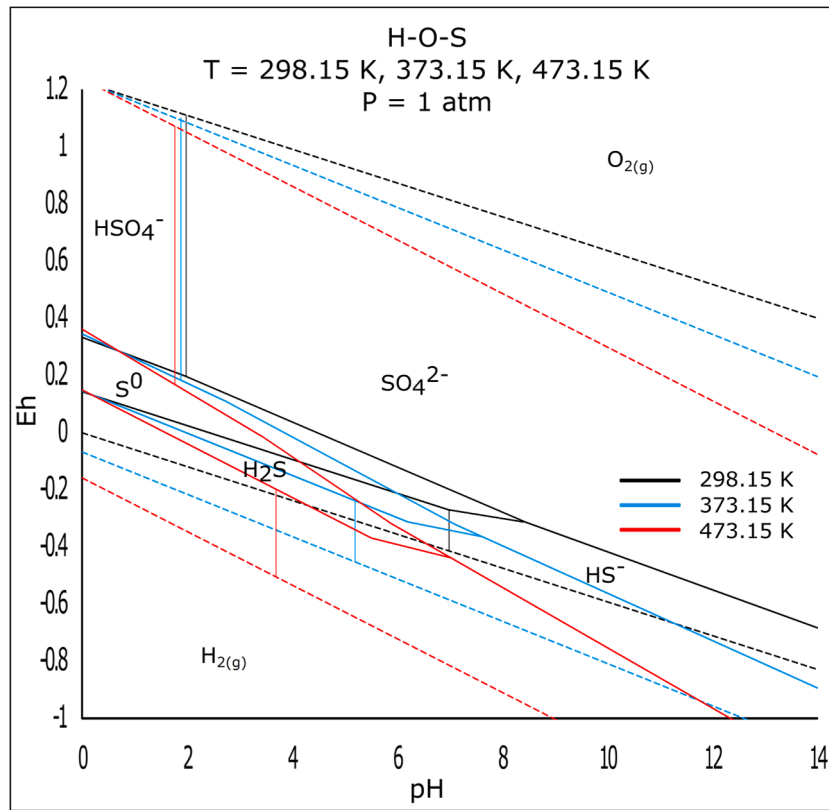


Fig. 3. H—O—S system at 1 atm and contours of 25 °C, 100 °C, and 200 °C at fixed ionic strength. The area between the dashed lines (O_2 and H_2) denotes the stability field of H_2O . The pressure contours are determined using μ_P and μ_o determined from IGL volumes. Species identifier markers are placed within its respective stability field at STP (same as in Fig. 2).

the notion that f_{O_2} is very low at modeled temperatures (Giggenbach, 1987). Temperature changes also affect a species' stability field. For example, at 25 °C, SO_4^{2-} is stable at pH 10 and Eh 0.4 V. If the temperature is increased to 200 °C, SO_4^{2-} is now the stable species at pH 10 and Eh -0.4 V. The increase in temperature has shifted the stability field of SO_4^{2-} to where the dominant species previously was in the more reduced HS^- form.

3.2.4. Eh-pH stability fields at non-standard pressure

A gaseous fluid within a geothermal reservoir will not have the same volume as it would at the surface under 1 atm pressure. For a uniform vertical pressure gradient of ~25 MPa/km (e.g., 24.3 MPa/km (Kruszewski et al., 2021, <23.1 MPa/km (Chatterjee et al., 2015)), the pressure exerted on fluid may exceed the critical points of its constituent gasses. Supercritical fluids are more probable in conductive-low temperature geothermal systems, which, due to their smaller temperature gradient, necessitate that the EGS be located deeper. Eh-pH calculations and diagrams are still valid for such situations; however, the change in pressure needs to be accounted for as it directly alters the Gibbs free energy and, thus, the equilibrium of a reaction. The chemical potential denoted as (μ) is equal to the Gibbs free energy (Pourbaix, 1949, 1950; Smith et al., 2013; Chen, 2019) and is effectively the energy density (E/mol). This connection, written as

$$\mu = \Delta G \quad (23)$$

allows for the reservoir pressure to be considered. The Gibbs free energy at STP is the datum from which the chemical potential at reservoir pressure is compared (Smith et al., 2013). After the substitution of μ for ΔG , and for a constant temperature, the chemical potential along with its relation to pressure is given in the following equations from Smith et al. (2013) as

$$\Delta G_r(P) = \mu_P - \mu_o, \quad (24)$$

and for a pure species in a homogenous fluid,

$$RT \ln(\phi) = RT \ln\left(\frac{f}{P}\right) = \int_{P_0}^{P_1} \left(\frac{V}{P} - \frac{RT}{P}\right) dP. \quad (25)$$

Where, μ_P and μ_o are the chemical potentials for the reservoir gas (often referred to as real gas) at pressures (in MPa) P_1 and the ideal gas at P_0 , respectively. Recall that $\mu_o = \Delta G_r^o$ and is available in thermodynamic tables (298.15 K and 1 atm (Bakker, 2012)). The fugacity coefficient is symbolized as ϕ , and is taken as unity at 1 atm (Smith et al., 2013). The molar volume for a pure gas is given as V (in cm^3/mol). After integration of the right side of Eq. (25) across the pressure domain, it can be merged with Eq. (24), yielding

$$\Delta G_r(P) = \left(\frac{VP}{P} - RT \ln(P)\right)_{P_1} - \left(\frac{VP}{P} - RT \ln(P)\right)_{P_0} - \mu_o. \quad (26)$$

If Eq. (26) is evaluated where P_1 is taken at STP then there is no difference between the chemical potentials and thus

$$\Delta G_r(P) = \mu_o. \quad (27)$$

Similarly, sufficiently low-pressure fluids will approach a fugacity of unity because their volume approaches the same volume of an ideal gas at 1 atm. Mixed fluids are treated using the same approach as in Eq. (24), but the partial volume of a species is instead the molar fraction, denoted as \bar{V}_i (Smith et al., 2013) and is given by

$$RT \ln(\phi) = RT \ln\left(\frac{f}{P}\right) = \int_{P_0}^{P_1} \left(\frac{\bar{V}_i}{P} - \frac{RT}{P}\right) dP. \quad (28)$$

Pressurized geothermal fluids are not single-phase fluids (unless they are supercritical) but will contain both gas and liquid states (Yanagisawa et al., 2021). Therefore, Eq. (28) is more appropriate for modeling such pressurized fluids. The effect of near ambient pressures on the H—O—S system is provided in Fig. 4.

For a constant temperature of 25 °C, species' stability field contour lines are obtained for pressures of 2 atm, and 4 atm are compared against those obtained at 1 atm. The ideal gas law (IGL) was used to model the volume change; because of this, the stability field diagram represents a qualitative estimate of the species present. A more robust approach would be to consider alternative equations of state (EOS) (see Section 3.2.5). Nonetheless, Fig. 4 provides a proof of concept and illustrates that the change in chemical potentials and equilibrium boundaries is minimal at the pressures considered. Additionally, as pH-Eh diagrams are given at 25 °C and 1 atm (Garrels and Christ, 1965; Brookins, 1986, 1988; Takeno, 2005) this serves as a good datum for comparison at relatively low pressures. However, there is a noticeable change in equilibrium boundaries for the H_2S - HS^- and HSO_4^- - SO_4^{2-} species. As pressure is increased, the $\Delta G_r(P)$ of all reactions is reduced, indicating that the reaction approaches spontaneity or becomes more spontaneous. The most significant changes are observed for the species involved in the two aforementioned equilibrium reactions. The stability fields of SO_4^{2-} and HS^- are shifted to lower pH domains. It is not immediately clear why these boundaries are the most sensitive to pressure changes or what physical phenomenon is causing this effect. One speculation may be that increased pressure reduces the degassing of acidic species and maximizes the H^+ in an aqueous solution. One observation is that the most prominent effects are observed for aqueous-gaseous species. Moreover, equilibrium contour lines involving solid sulfur (as $\text{S}^0_{(s)}$) exhibit negligible change, even at P of 4 atm (Fig. 4). Our observation is confirmed by a previous study by Brookins (1988), where free energies of reactions involving aqueous or solid phases were minimally altered by increased pressures.

3.2.5. Advancing electrochemical modeling in geothermal systems

Modeling (high pressure) non-ideal fluids are well-established at surface-level geothermal power plants utilizing ORC for the production of electricity (Rodríguez et al., 2013; Cammarata et al., 2014; Liu et al., 2014; Kazemi and Samadi, 2016). However, modeling supercritical fluids within the geothermal reservoir and the effect of pressure on Eh represents a gap in the literature regarding fluid-rock interaction. Yanagisawa et al. (2021) state that software modeling of supercritical geothermal fluids is hindered by unavailable data. This gap is present both in geothermal fluids and groundwater studies. If the total pressure is not considered, then V or \bar{V}_i will be inaccurate. This leads to erroneous chemical potentials and, ultimately, incorrect Eh values. This, in turn, may result in inaccuracies in modeling fluid-rock behavior and inaccurate reservoir predictions. In the literature, pressure is ignored, not explicitly mentioned, or taken as 1 atm for samples that may or may not be at atmospheric pressure. While the computer program WATCH (Arnórsson et al., 1982) is well-suited for hot spring geothermal fluids at the surface, it is unfortunately not designed to handle deep reservoirs at high pressure. Studies of surface-level hot springs at 1 atm do not consider V or \bar{V}_i (Stefánsson and Gíslason, 2001; Pope et al., 2004). Andrews and Kay (1983) report pCO_2 in their assessment of groundwater Eh. Using the reported depth and temperature of ~ 1680 m and ~ 71 °C, the resulting total pressure is ~ 34 MPa (using a modest pressure gradient of 20 MPa/km). This far exceeds the critical point of CO_2 (7.38 MPa and 31.1 °C)-indicating that the CO_2 is indistinguishable from any liquid, thus rendering \bar{V}_i incalculable. In addition, this gas would behave non-ideally, and the standard IGL would be inappropriate. Instead, an alternate EOS should be utilized for meaningful V or \bar{V}_i . There are many EOS available for modeling non-ideal fluids (some examples include but are not limited to that given by van der Waals (1873), Redlich and Kwong (1949), Lee and Kesler (1975), and Peng and Robinson (1976). These EOS models will likely provide more accurate μ_p

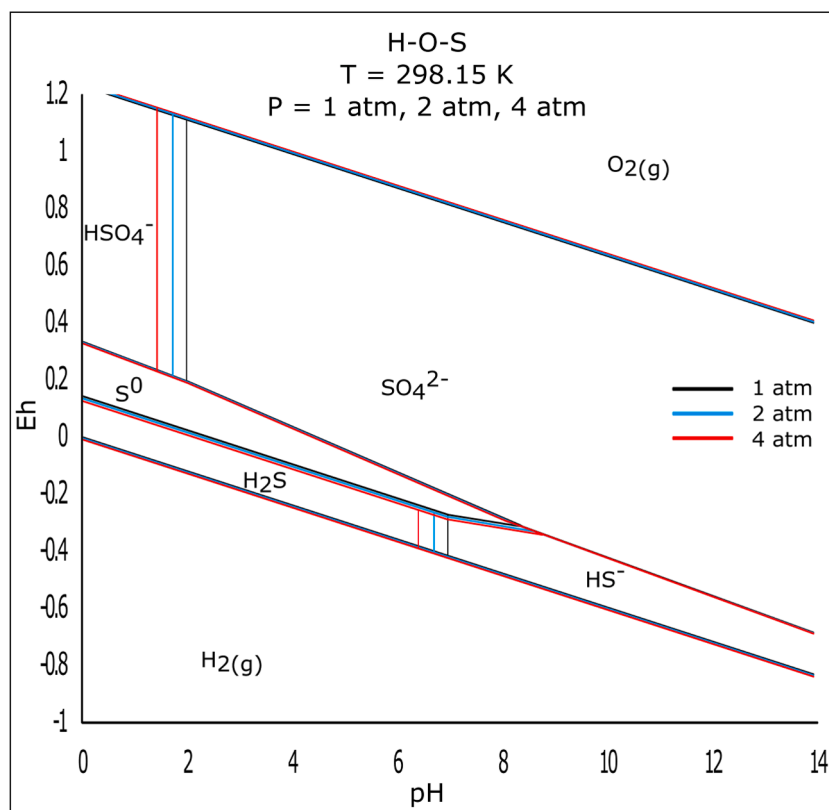


Fig. 4. H—O—S system at 25 °C and contours of 1 atm, 2 atm, and 4 atm found using the IGL at fixed ionic strength. The pressure contours are determined using μ_p and μ_o determined from IGL volumes. Species identifier markers are placed within its respective stability field at STP (same as in Fig. 2).

values of high-pressure geothermal fluids. The use of models for non-ideal fluids alongside the inclusion of heat capacity species data would expectedly yield more accurate Eh data.

3.3. Dissolution kinetics

It is crucial to consider dissolution alongside scaling as both are intimately linked, particularly for equilibrium reactions. Neither of these processes necessarily proceeds the other, as precipitation requires that some dissolution must have occurred elsewhere to supply the ions needed for precipitation. Similarly, the ions in the solution must have been derived from a solid source. The rate of dissolution also affects the rate of ions entering the solution and is therefore linked to the rate of saturation. A geothermal fluid may become supersaturated with respect to some scaling mineral, but if the rate of dissolution supplying the necessary ions is low, supersaturation will be achieved commensurately slowly.

As noted in Section 3.1, the Eh of a fluid may or may not be in electric equilibrium. If the redox state of the fluid is not in equilibrium, then the measured value will only pertain to that instance in time (dt). Similarly, the pH of a fluid is a controlling variable in the rate of dissolution (Section 2.1.1). Fig. 5A illustrates that r is affected by not only pH but also temperature. For a dilute solution, the γ_i values of acid are taken as 1, thus $a_{H^+}^+ = [H^+]$. The rate of dissolution certainly increases with an increase in temperature; however, for mineral equilibrium reactions that include a gaseous species, an increase in temperature may lead to gas exsolution-causing supersaturation, leading to precipitation (Given and Wilkinson, 1985). For example, consider carbonate minerals; boiling would reduce the dissolved CO_2 (Ellis, 1979; Arnórsson, 1989), thus actually increasing pH due to a loss of carbonic acid production-leading to less H^+ and a slower dissolution rate. Precipitation of calcite may also occur if the pressure exerted on the fluid is reduced (Holland and Malinin, 1979; Tulloch, 1982), thereby allowing for dissolved CO_2 to exsolve and enter the gas phase (Chen et al., 2016). Fig. 5B compares the

rate of calcite and dolomite at a constant temperature to illustrate the effect of k for each mechanism as well as the n in the $a_{H^+}^n$ term. Since calcite dissolves faster than dolomite, a geothermal fluid would become saturated with respect to calcite before dolomite.

We propose that the total dissolution (TD) is simply the integrated dissolution rate at some pH (r_{pH_n}) over some time interval (TD(t)) and may be determined as

$$TD(t)_{pH_n} = A + \int_{t_1}^{t_2} r_{pH_n} dt. \quad (29)$$

Note the sign convention, where $TD > 0$, yet, it is mass lost from the solid phase. If there has been no previous dissolution, $A = 0 \text{ mol/m}^2$. Comparison between fluids of static pH may be evaluated using our proposed Eq. (30) below. If, for example, a solution of static pH is allowed to dissolve calcite for 3600 s (1 h) at 50 °C, then,

$$TD(t)_{\frac{pH_x}{pH_y}} = \frac{\text{Total loss}_{pH_2}}{\text{Total loss}_{pH_4}} = \frac{\int_0^{3600 \text{ s}} r_{pH_x} dt}{\int_0^{3600 \text{ s}} r_{pH_y} dt}. \quad (30)$$

The TD of calcite at pH 2 would be $\sim 68 \text{ mol/m}^2$, while the total dissolved calcite at pH 4 would be $\sim 23 \text{ mol/m}^2$. If the pH of the solution is dynamic and monotonically increases at a constant rate from pH 2 to pH 4, then, for the same time interval, there are three r_{pH_n} , one for each pH value. The TD for such a fluid is approximated by rewriting Eq. (28) as,

$$\begin{aligned} TD(t)_{pH_x+pH_y+pH_z} &= TD(t)_{pH_2+pH_3+pH_4} \\ &= \left(\int_0^{1200 \text{ s}} r_{pH_x} dt \right)_{pH_2} + \left(\int_{1200 \text{ s}}^{2400 \text{ s}} r_{pH_y} dt \right)_{pH_3} \\ &\quad + \left(\int_{2400 \text{ s}}^{3600 \text{ s}} r_{pH_z} dt \right)_{pH_4} \end{aligned} \quad (31)$$

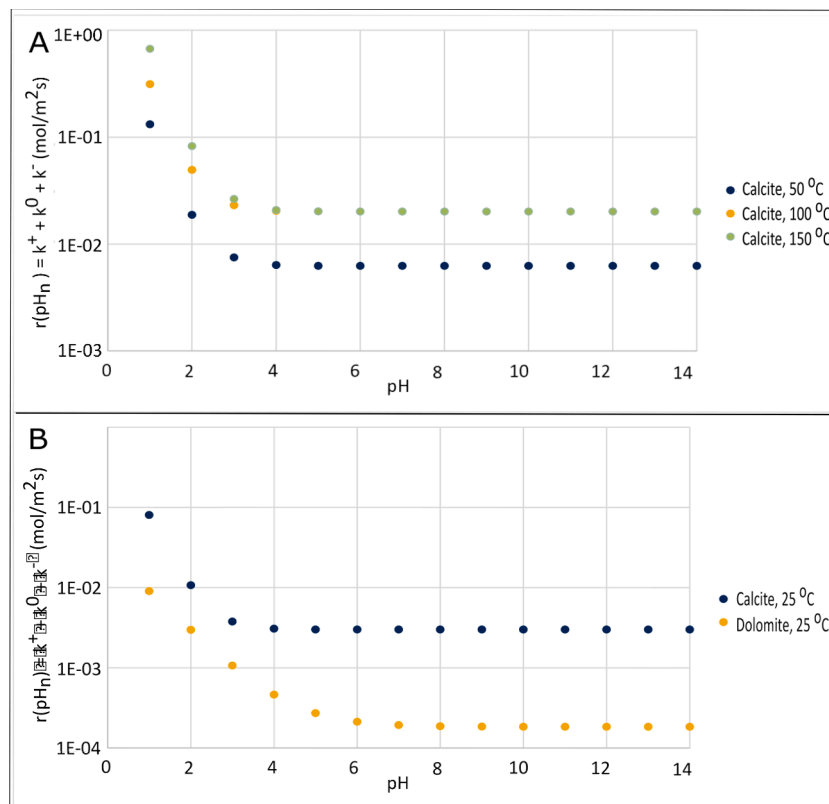


Fig. 5. Dissolution rates (r_{pH_n}) of calcite and dolomite using data from Palandri and Kharaka (2004). (A) Calcite dissolution as a function of pH at constant T of 50 °C, 100 °C, and 150 °C. (B) Comparison of dissolution rates for calcite and dolomite at 25 °C, $n_{\text{calcite}} = 1$, and $n_{\text{dolomite}} = 0.5$.

In this case, the TD of calcite obtained using Eq. (31) is $\sim 39 \text{ mol/m}^2$ and is 58% of the total dissolved calcite at pH 2. The reason that r is not the average between the end members ($\sim 45 \text{ mol/m}^2$) is because r is not evenly distributed across the pH domain but is instead skewed (Fig. 5A). The r (as r_{pH_3} to r_{pH_4}) for the time interval encompassing pH 3 to pH 4 ($1201 \leq t \text{ (s)} \leq 3601$) is closer to r_{pH_4} . This indicates the overall r is more heavily weighted towards lower rates than evenly split into thirds. The dissolution rate continues to slow proportional to pH and is directly related to Ω . The Bjerrum plot indicates that as pH increases, Ω will also increase (high $a\text{CO}_3^*$). At equilibrium (Eq. (1)), the forward dissolution reaction rate equals the reverse precipitation rate, and the net r is zero. It is worth noting that the total dissolution in Eq. (31) is an estimation and assumes that each step in pH occurs instantaneously and is held constant for 1200s. A more realistic consideration for the pH evolution of a natural geothermal fluid would include many more time intervals; ideally, for a continuously evolving fluid, one r_{pH_n} for each dt. Finally, as the pH range of 2 to 4 given above was selected primarily to illustrate the effect of pH on dissolution kinetics, the acidity of natural systems have been shown to change rapidly (four days) from pH 2.82 to 5.36 at $\sim 90^\circ \text{C}$ (Fournier et al., 1992). Therefore, the dissolution rate profile in Fig. 5A (100 °C curve) would reasonably track this pH evolution over time.

The direct effect of pH on the I.S. of a solution is minimal; that is, the contribution of hydronium ion ($[x_i]z_i^2$ for H^+ in Eq. (5) is minimal. However, the effect of pH on the saturation state of a mineral is tremendous. Acidic solutions increase the TDS, (thereby also raising I.S.) which may change the saturation state of the fluid. The effect of pH on kinetics is similar, as more $[\text{H}^+]$ will result in a greater total amount of mineral dissolution over a time interval, possibly causing a feedback loop where saturation is reached faster due to the increase in IAP for that mineral. This feedback loop is exacerbated when the temperature is increased.

4. Corrosion and scaling in geothermal systems

Specific forms of corrosion and an illustrative example of calcite scaling are considered below. Additional common scale-forming minerals are outlined below along with the pH-Eh stability fields of these mineral phases and treatments.

4.1. Corrosion

Corrosion is detrimental to EGS operations. Damaged materials and power plant downtime leads to reduced efficiency and are economically problematic (Karlsdottir et al., 2019). Moreover, since geothermal fluids are often at high temperatures and pressures, corrosion can lead to potentially highly dangerous operating conditions (Mundhenk et al., 2019). The corrosion rate is highly similar conceptually to dissolution, and as a kinetic rate (Mundhenk et al., 2019), it is directly related to pH. Corrosion rates have also been shown to increase with temperature (up to 320°C as in Yanagisawa et al., 2021)-reiterating the effect of temperature on kinetics. The rate of corrosion is simply the mass lost per unit of time and can be determined using the following equation after ASTM (2017),

$$\text{Corrosion Rate} = \frac{KW}{ATD} \quad (32)$$

where K is a constant (is equal to 8.76×10^4 if mm/year is used), W is the material mass that has been removed from the exposed surface (g), A is the exposed surface area (cm^2), T is the time that the material has been exposed (hr), and D is the material density (g/cm^3)- available for many steel grades from ASTM (2017). The relation of corrosion to Eh is quite clear; Pourbaix (1950) devised a graphical model to predict the likelihood of corrosion in pH-Eh space. Corrosion occurs when the exposed reactive surface metal of a material enters the solution as an ion and is caused by a redox reaction, thereby increasing its concentration in the

fluid (Pourbaix, 1950). For example, consider the oxidation half reaction of solid iron,



The Gibbs free energy of this equation is negative (-9.54 kcal/mol at 298.15 K), indicating that elemental iron will spontaneously oxidize (corrode), and the forward reaction is thermodynamically preferred (e. g., CRC, 2017). The corrosion of steel, shown below as an oxidation reaction in the presence of acid after Diamond and Alt-Epping (2014) is (electrons have been added for clarity),



The inclusion of acid releases more energy, and the reaction becomes more spontaneous (-18.8 kcal/mol at 298.15 K). In both examples, the transfer of electrons from solid iron to dissolved iron results in an increase in the concentration of Fe^{2+} in the solution. The mass transferred into the solution equals the mass lost from the solid phase. Therefore, the corrosion rate is a direct reflection of the transfer of electrons (redox reactions) from the metal cation on the reactive surface of the steel to the electron acceptor in the fluid. Some ions and molecules present in geothermal fluids that are noted to contribute to corrosion are referred to as the total key species (TKS). Ellis and Conover (1981) state that the TKS is obtained using;

$$\text{TKS} = \sum ([\text{Cl}^-], [\text{CO}_3^{2-}], [\text{HCO}_3^-], [\text{H}_2\text{S}], [\text{NH}_3], [\text{SO}_4^{2-}]) \quad (35)$$

where the units of concentration are in ppm. Arvanitis et al. (2020) further expanded the TKS to include all sulfide and ammonia species. The pH, Eh, and TKS (which themselves are pressure and temperature-dependent) are important variables that control corrosion, and geothermal reservoirs are unique and have unique fluid chemistries. Despite this, geothermal fluids can be grouped according to their corrosivity class. There are six fluid classes, and their defining characteristics are provided in Table 1 (from Nogara and Zarrouk 2018a; and references therein). Nogara and Zarrouk (2018a; 2018b) offer an excellent two-part review on corrosion in geothermal systems. It is our intention below to provide recent updates since their contribution mainly. Finally, there is a tremendous lack of consistency regarding steel names (e.g., AISI/SAE, ASTM, or UNS), which results in unwieldiness and confusion. Considering that there are thousands of grades of steel available (Baciu et al., 2020) it would be beneficial to for the community to adopt a consistent format. For example, Hua et al. (2021) conducted corrosion experiments on 3Cr steel, but this specific steel grade name does not appear to be indexed in any of the databases mentioned above.

4.1.1. Uniform corrosion

Uniform corrosion is most pervasive in carbon steel (e.g., S235JR)

Table 1

Comparisons of the six corrosion classes of geothermal fluids. NCG refers to non-condensable gasses. Nogara and Zarrouk (2018a) include CO_2 , total ammonia, and total sulfide in TKS summation.

Class	Case Study Example	TKS (ppm)	pH	Notes
I	Salton Sea, USA	>100,000	<5	99% of TKS is Cl^-
II	Matsukawa, Japan	1000 to 10,000	<4.5	liquid-dominant fluid
III	Cerro-Prieto, Mexico	10,000 to 20,000	5 to 6	near neutral pH
IV	Broadlands, New Zealand	500 to 10,000	≥ 5	liquid-dominant fluid
V(a)	Pagosa Spring, USA	<5000	6.7 to 7.6	low T, lower pH than V (b)
V(b)	Klamath Falls, USA	<5000	7.8 to 9.5	low T, higher pH than V (a)
VI	Geysers, USA	–	–	vapor-dominant fluid, <5 wt% NCG

compared to either austenitic stainless steel (UNS S31603) or duplex stainless steel (UNS S31803) (Faes et al., 2019). This observation is supported by Arvanitis Arvanitis et al. (2020), who noted that 316 stainless steel is deemed an appropriate material to use to mitigate uniform corrosion in EGS operations. Carbon steel can be used as material if the thickness is sufficient, although as this material is susceptible to uniform corrosion, the thickness will have to be monitored to ensure safety (Faes et al., 2019). Unfortunately, these workers did not provide information regarding the thickness required for safe operation and conducted their experiments at only 0.5 MPa. Therefore, future work should address the carbon steel wall thickness:pressure relationship at a higher pressure for safe EGS power plant operation.

The vapor-dominant fluid (containing both CO₂ and H₂S gasses) at the Reykjanes geothermal site in Iceland would be classified as Type VI (Table 1) (Hardardóttir and Oskarsson, 2017). High entropy alloy (HEA) AlCrFeNiMn steel experienced a uniform corrosion rate of 3.25 mm/year when exposed to this type of fluid and is, therefore, not a recommended material (Karlsdóttir et al., 2019).

Yue et al., 2021 observed multilayering on the surface of super 13Cr steel consisting of an outer and mid layer of FeCO₃ and FeCr₂O₄, respectively. Hua et al. (2021) conducted similar experiments and also observed the same multilayering in 3Cr steel, as well as an interesting relationship between pCO₂ and corrosion. In their study, they observed that an increase in pCO₂ offers increased corrosion resistance on the exterior of the 3Cr steel by forming a FeCO₃ shield and mid-layer of FeCr₂O₄, but simultaneously increases localized corrosion directly against the 3Cr steel (below the FeCO₃ shield).

4.1.2. Pitting corrosion

The ability of a steel to resist pitting corrosion is related to the quantity of Cr, Mo, and N in its alloy and may be assigned a number referred to as the pitting resistance equivalence number (PREN) using the equation below (e.g., Garfias-Mesias et al., 1996; Nikitasari et al., 2019; Zhang et al., 2022).

$$PREN = \%Cr + 3.3 \%Mo + 16 \%N, EQ. 36 \quad (36)$$

where the weight percent of each metal are used to determine the PREN of the material. Nikitasari et al. (2019) found a relationship between PREN and the pit diameter in CA6NM steel as

$$\bar{d} \propto \frac{1}{\alpha} (\%Mo + \%N) \quad (37)$$

where \bar{d} is the average pit diameter. The calculated TKS from these workers reported brine composition indicates that a Class I fluid type is the best fit.

Austenitic steel UNS S31603 and duplex steel UNS S31803 are susceptible to pitting corrosion at highly oxidizing conditions (anodic sweep) (Faes et al., 2019). Pitting corrosion can serve as a nucleation site for another type of corrosion, stress corrosion cracking (SCC, Section 4.1.3) (Qi et al., 2021). Yue et al. (2021) observed an increase in localized pitting corrosion when the super 13Cr steel sample was rotated within the fluid bath compared to pitting corrosion under no rotation. This implies that pitting corrosion in quiescent tanks or tubing in geothermal power plants would be more severe than in a similar vessel containing a turbid fluid. Recently, Zhang et al. (2022) found high pitting corrosion resistance in FCWA-AM duplex steel (PREN up to 47.53), which performed similarly to the hot-rolled 2205 steel, and both performed favorably to the E2209 duplex steel in polarization curve testing. These workers attribute much of the pitting corrosion resistance to the abundance of intragranular austenite (IGA) throughout the FCWA-AM steel.

4.1.3. Stress cracking corrosion

According to Nogara and Zarrouk (2018a), stress corrosion cracking may take three forms; chloride-SCC, ammonia-SCC, and sulfide-SSC.

Corsi (1986) differentiates SCC from SSC and considers them separately. In either case, both of these workers note that SSC is prone to occur in high tensile strength stainless steel. This form of corrosion is the most dangerous. Unlike uniform corrosion occurring on the exposed surface, SCC can penetrate the material (Chang et al., 2019) and cause catastrophic failure (e.g., NDK explosion in 2009, see Zhang et al., 2016). The safest operation would be to ensure that the geothermal fluid does not have pH-Eh coordinates, which plot in the O₂ stability field, or the H₂S or HS⁻ stability fields (Figs. 2–4). This implies that a safer stability field for the geothermal operation would be in the SO₄²⁻ zone. Qi et al. (2021) observed a close relationship between pCO₂ and temperature. These workers do not give the fluid classification; however, the calculated TKS and relative abundance of Cl⁻ from their data suggests that Type I fluid (Table 1) is most suitable. Moreover, Qi et al. (2021) note that an increase in either of these variables results in increased susceptibility of HP-13Cr stainless steel to SCC. Recall that increased CO₂ will also lower the pH of the fluid, thus possibly shifting the pH-Eh coordinates from a stability field of a less hazardous species (SO₄²⁻) to a more hazardous stability field (H₂S or HS⁻).

4.1.4. Galvanic corrosion

Stoljarova et al. (2021) compared ST37 carbon steel to 1.4404 Cr stainless steel and 1.4562 Ni stainless steel in an artificial brine (our calculated TKS indicates that the brine is closest to Class I) enriched in Cu and Pb. These workers note that the two stainless steel materials exhibited zero uniform or pitting corrosion, while the carbon steel was determined to be a poor material choice for geothermal operations.

4.2. Scaling

Scaling occurs when the constituent ions of a mineral overcome (IAP) the carrying capacity of the fluid (solubility) and become supersaturated (Söhnel and Garside, 1992). Scaling is problematic in geothermal (or industrial, e.g., Söhnel and Garside, 1992) systems as it reduces operational capability (Miller, 1980) and can be destructive to and reduce the lifespan of the power plant (Zotzmann and Regenspurg, 2015). The degree to which a mineral phase is likely to precipitate and form a scale can be modeled using saturation indices (SI). The SI value is a valuable number that is used to evaluate the likelihood of scaling. If the propensity of scaling is high, measures can be taken to mitigate such scaling (See Table 2 in Section 4.3) (Stahl et al., 2000). The basic SI Ω value (Eqs. (2), (38), and (42)) can be evaluated for any mineral; however, some mineral-specific SI (e.g., LSI and I_s Section 4.2.1) is not transferrable.

As EGS frequently contains carbonate rocks (Hofmann et al., 2014; Moeck, 2014; Schütz et al., 2018) and calcite (in particular), precipitation leads to adverse scaling effects (Phillips et al., 1977; Corsi, 1986; Gunnlaugsson et al., 2014), and is highly common (Simmons and Christenson, 1994; Pátzay et al., 1998; Antony et al., 2011; Gunnlaugsson, 2012; Finster et al., 2015; Zolfaghroshan and Khamehchi, 2020; Bu et al., 2022) it will be used as an example in the preceding pH examples. Finally, scaling enhances corrosion (Söhnel and Garside, 1992), thus, scale management improves not only efficiency but also reduces corrosion.

4.2.1. Saturation indices

Pitzer and Mayorga (1973) proposed a model for calculating activities for single electrolyte solutions (up to 6 M). Although geothermal fluids often contain high I.S., this model fails somewhat in its application since geothermal fluids are compositionally complex and contain many dissolved species, and are not at STP conditions. Moreover, K_{sp} varies not only with temperature but also with the solution composition (e.g. Chong and Sheikholsami, 2001). To address this, Sheikholsami (2005) devised the potential scaling index (SPI), which utilizes the Gibbs free energy of reaction found in Pitzer and Mayorga (1973) used for high I solutions. The SPI was later adapted by Sim et al. (2018), as

Table 2

Common scaling minerals encountered in geothermal systems. If available, pH and Eh values where such minerals are present as solid scales are given. If no explicit data is available, qualitative interpretations of preexisting data is given (i.e. “oxidizing”). Additionally, if available, pH-Eh data for the anion in the mineral or solid phase (PO_4^{3-} and SO_4^{2-}) is included. Techniques for scale mitigation and complications that may arise due to scale treatment are also provided. Numbered exponents in parentheses pertain to references; (1) [Filmtec, 2023](#); (2) [Antony et al., 2011](#); (3) [Wheeland and Robertson, 1987](#); (4) [Ellis and Conover, 1981](#); (5) [Holland and Malinin, 1979](#); (6) [Tulloch, 1982](#); (7) [Gallup, 2011](#); (8) [Henley, 1983](#); (9) [Gallup et al., 1995](#); (10) [Utami et al., 2014](#); (11) [Setiawan et al., 2019](#); (12) [Ngothai et al., 2012](#); (13) [Petro et al., 2013](#); (14) [Macdonald, 1980](#); (15) [Diamond and Alt-Epping, 2014](#); (16) [Hall, 1986](#); (17) [Carbonell et al., 1999](#); (18) [Barnaby and Rimstidt, 1989](#); (19) [Takeno, 2005](#).

Mineral	pH	Eh	Additional Causes	Treatment Notes	Treatment Side Effects
Calcite	>8, Ca^{2+} present up to at least ~12 ⁽¹⁹⁾	Ca^{2+} not limited by Eh, stable in water ⁽¹⁹⁾	Depressurization ^(5,6)	HCl or H_2SO_4 acidification ⁽²⁾	Use of H_2SO_4 could lead to the precipitation of sulfate minerals ⁽²⁾ , use of HCl increases $[\text{Cl}^-]$, a TKS ⁽⁴⁾
Calcium phosphate (amorphous)	For PO_4^{3-} , pH > 12 ⁽¹⁹⁾	PO_4^{3-} not limited by Eh, stable in water ⁽¹⁹⁾		Ensure water pH < 12	
Gypsum	for SO_4^{2-} , pH 3 to 14 (Fig. 2)	SO_4^{2-} relatively oxidizing (Fig. 2)	$[\text{SO}_4^{2-}] > 3000 \text{ mg/L}^{(3)}$	Phosphate ester ⁽³⁾ concentration not provided, air bubbler ⁽³⁾ , pH < 3	
Illite			Low $\text{pCO}_2^{(13)}$	Introduce supercritical CO_2 . Illite solubility is increased in the presence of liquid or supercritical $\text{CO}_2^{(3)}$	
Iron, Manganese-oxides	Pyrolusite (MnO_2) stable at pH 5 to ≥ 9 , iron hydroxide ($\text{Fe}(\text{OH})_3$) stable at pH ~5 to ≥ 9 ⁽¹⁸⁾	Fe or Mn oxyhydroxides may precipitate at oxidizing conditions ⁽¹⁷⁾ . Pyrolusite stable from ≤ -0.4 to $> 0.8 \text{ V}$, iron hydroxide stable from ≤ -0.2 to $> 0.8 \text{ V}^{(18)}$	Fe, Mn metals are more soluble at lower Eh ⁽¹⁷⁾ , thus precipitation as oxides is likely at oxidizing conditions	Reducing agent, acidification	
Pyrite	pH 0 to ~12 ⁽¹⁴⁾	Scaling in heat exchanger ⁽¹⁵⁾ suggests oxidizing conditions, high or low $\text{fO}_2^{(16)}$, ~0 V ⁽¹⁴⁾		Solubility increases at high temperature	
Silica (amorphous)	Variable. Scaling inversely related to pH ⁽¹¹⁾ , solubility increases with pH > 7 ⁽¹²⁾ , scaling most pervasive at high pH ⁽¹²⁾	Oxidizing ⁽⁷⁾	$[\text{Al}^{3+}] + [\text{Fe}^{3+}] > 0.05 \text{ mg/L}^{(1)}$	High atomic mass unit polyacrylates ⁽¹⁾ , consumption of oxygen via formic acid ($\text{HCOOH}^{(7)}$), double-flash separation ⁽¹⁰⁾ , remove steam from liquid at surface ⁽⁸⁾ , acidification ⁽¹⁰⁾ , alkalization ⁽¹⁰⁾	Fluid reduction may lead to precipitation of Ag, As, Au and Sb ⁽¹⁰⁾ , pH < 4 is corrosive ⁽⁷⁾

$$SPI = \log \left(\left(\frac{[a_i][a_j]}{\exp\left(\frac{-\Delta G_{\text{reaction}}^{\circ}}{RT}\right)} \right)^{1/\nu} \right) \quad (38)$$

In the case of calcite, the numerator is the IAP of the Ca^{2+} and CO_3^{2-} , the $1/\nu$ exponent is the sum of the stoichiometric cations and anions ($1 \text{ Ca}^{2+} + 1 \text{ CO}_3^{2-} = 2$, so $1/\nu = 1/2$), R is the gas constant, T is temperature in Kelvin, and $-\Delta G_{\text{reaction}}^{\circ}$ is,

$$\Delta G_{\text{reaction}}^{\circ} = \Delta G_{\text{products}} - \Delta G_{\text{formation}} = \left(\Delta G_{\text{Ca}^{2+}(\text{aq})} + \Delta G_{\text{CO}_3^{2-}(\text{aq})} \right) - \Delta G_{\text{calcite}}, \quad (39)$$

although a general form would be written as

$$\Delta G_{\text{reaction}}^{\circ} = \Delta G_{\text{products}} - \Delta G_{\text{formation}} = \left(\Delta G_{x_{(\text{aq})}^{z+}} + \Delta G_{y_{(\text{aq})}^{z-}} \right) - \Delta G_{\text{mineral}}, \quad (40)$$

It is important to note that if units of Gibbs free-energy are kcal/mol, then R is 1.987×10^{-3} kcal/mol. As K_{sp} varies with temperature, then after [Sim et al. \(2018\)](#), solving for $K_{\text{sp}}(T)$ yields

$$K_{\text{sp}}(T) = \exp\left(\frac{-\Delta G_{\text{reaction}}^{\circ}}{RT}\right). \quad (41)$$

The Supersaturation ratio (S_r) is another general saturation index. It is similar to the basic Ω found in [Eq. \(7\)](#), but incorporates the $1/\nu$ exponent like the SPI model and is expressed as (e.g. [van de Lisdonk et al., 2001](#); [Sim et al., 2018](#))

$$S_r = \left(\frac{[a_i]^{v+}[a_j]^{v-}}{K_{\text{sp}}(T)} \right)^{1/\nu} \quad (42)$$

Note that the ion activities above in the numerator have been simplified from the given $(\gamma_{+}c_{+})^{v+}$ $(\gamma_{-}c_{-})^{v-}$ provided by the aforementioned workers. The $+v$ and $-v$ are the stoichiometric numbers of cations and anions in the equilibrium reaction. Using CaF_2 as an example, $+v$ is 1 Ca cation, and $-v$ is 2 F anions, yielding v of $1 + 2 = 3$ (eg. [van de Lisdonk et al., 2001](#)).

Calcite-specific saturation models such as the Langelier Saturation Index (LSI) ([Langelier, 1936](#)) have been applied to geothermal fluids ([Pátzay et al., 1998](#); [Rafferty, 1999](#); [Varga et al., 2019](#)). This model is valid for $10 < \text{TDS} (\text{mg/L}) < 10,000$ ([Sim et al., 2018](#)), and for pH ranging from 7.0 to 9.5 ([Langelier, 1936](#)). It is presented as,

$$LSI = \text{pH} - \text{pH}_s. \quad (43)$$

Where pH_s is the pH of saturation with respect to calcite. The LSI does not quantify the mineral saturation of a solution but rather indicates if dissolution ($LSI < 0$) or precipitation ($LSI > 0$) are expected ([Sim et al., 2018](#)). This model has been presented in various alternate forms (e.g. [Sim et al., 2018](#)); however, the proceeding form is after [Sheikholeslami \(2005\)](#), where the ion concentrations are in units of mg/L, as;

$$\text{pH}_s = \text{p}[\text{Ca}^{2+}] + \text{p}[\text{HCO}_3^-] + \left(9.3 + \frac{\log(\text{TDS}) - 1}{10} - 13.12 \log(T) + 34.95 \right). \quad (44)$$

[Sheikholeslami \(2005\)](#) notes that while the LSI is a familiar

saturation index model, it is not designed for high TDS solutions-as are observed in many EGS reservoirs. Moreover, since the model is limited to $\text{pH} > 7.0$, then the high pressures associated at great depths (particularly for conduction-dominant EGS reservoirs) would force the relatively elevated pCO_2 into $[\text{CO}_2]$, driving down pH , likely outside of the range suitable for the LSI model. Furthermore, the logistics associated with EGS reservoirs make high-quality *in-situ* pH measurements impossible (Oddo and Tomson, 1982).

Corsi (1986) provides a calcite-specific saturation index model modified from Oddo and Tomson (1982). This model requires neither activities, $K_{\text{sp}}(T)$, or pH in its calculation and does not utilize activities for Ca^{2+} or HCO_3^- , which may yield inaccurate Ω values at high I.S. However, this model accounts for both total system pressure and pCO_2 , which, when dissolved in the aqueous phase, is proportional to $[\text{H}^+]$. Moreover, the abundance of carbonic acid and its dissociation will contribute to the TDS of the solution. One advantage of this SI is its incorporation of pCO_2 . Calcite saturation decreases and becomes more soluble at higher pressures due to Henry's Law, but CO_2 boils more rapidly at higher temperatures, thereby increasing calcite saturation. Corsi (1986) provides this model in the following form

$$I_s = \log\left(\frac{[\text{Ca}^{2+}][\text{HCO}_3^-]^2}{PX\text{CO}_{2\text{g/aq}}}\right) + 10.22 + 2.739 * 10^{-2}T - 1.38 * 10^{-5}T^2 - 1.079 * 10^{-8}P - 2.52\sqrt{I} + 0.919I. \quad (45)$$

One disadvantage of the I_s model is that it uses concentration instead of activity; this would be a particular problem when modeling geothermal fluids of high I.S. (ionic strength written as I by the author). Corsi (1986) notes that alkalinity is "mainly given" as $[\text{HCO}_3^-]$, while the temperature is in $^{\circ}\text{C}$, and the total pressure is in Pa. Since CO_2 directly reduces the pH of the solution (Perkins, 2003), it is necessary to consider it in calcite saturation. XCO_2 is the mole fraction of CO_2 in the gaseous to the aqueous phase and obeys Henry's Law (K_{H}^{CC}). Henry's Law is an equilibrium concept, and as such, its values vary with temperature. The equations for calculating the temperature-corrected XCO_2 are (from Sander (2015);

$$\left(H(T)_{\text{aq/gas}}^{\text{cp}}\right)_{\text{VH}} = H_{\text{aq/gas}298.15\text{K}}^{\text{cp}} \exp\left(\frac{d\ln H}{dT}\left(\frac{1}{T} - \frac{1}{T_{298.15\text{K}}}\right)\right), \text{ then} \quad (46)$$

$$\left(\text{XCO}_{2\text{gas/aq}}\right)_{\text{VH}} = \left(K_{\text{Hgas/aq}}^{\text{CC}}\right)_{\text{VH}} = \frac{1}{H_{\text{aq/g}}^{\text{CC}}} = H_{\text{aq/gas}}^{\text{CC}} = H(T)_{\text{aq/gas}}^{\text{cp}} RT. \quad (47)$$

Note that $H_{298.15\text{K}}^{\text{cp}}$ is in $(\text{mol}/\text{m}^3\text{Pa})$, T is in (K) , R is in $(\text{in } \text{m}^3/\text{PaKmol})$, and H^{CC} is dimensionless. Sander (2015) cautions that the Van't Hoff expression is used to calculate $H(T)_{\text{VH}}$ in Eq. (46) is valid for limited temperatures, and an empirical approach is instead preferred. Bieling et al. (1989) performed an iterative optimization method to effectively obtain $H(T)$ in which the temperature range was later extended by Rumpf and Mauer (1993) using experimentally obtained data to 200°C , and then extrapolated again to 250°C with good results by García et al. (2006). The $H(T)$ equation from Rumpf and Mauer (1993) is

$$\ln\left(H(T)_{\text{gas/aq}}^{\text{1/cp}}\right)_{\text{RM}} = 192.876 + \frac{-9624.4}{T} + 1.441 * 10^{-2}T + (-28.749 * \ln(T)). \quad (48)$$

Note that the units in Eq. (48) are MPakg/mol , making it $1/\text{H}^{\text{cp}}$. We have solved for $H(T)_{\text{RM}}$, provided a conversion to the same units as in the Van't Hoff ($H(T)_{\text{VH}}$), and given a solution to $(\text{XCO}_2)_{\text{RM}}$, respectively as

$$\left(H(T)_{\text{gas/aq}}^{\text{1/cp}}\right)_{\text{RM}} = \exp(\ln(H(T)_{\text{gas/aq}}^{\text{1/cp}})_{\text{RM}}), \text{ then converting units by Eq. 48}$$

$$\left(H(T)_{\text{gas/aq}}^{\text{1/cp}}\right)_{\text{RM}} \frac{\text{kgMPa}}{\text{mol}} \rightarrow \frac{0.001\text{m}^3}{\text{kg}} * \frac{10^6\text{Pa}}{\text{MPa}} \rightarrow \left(H(T)_{\text{gas/aq}}^{\text{1/cp}}\right)_{\text{RM}} \frac{\text{m}^3\text{Pa}}{\text{mol}}, \text{ and} \quad (49)$$

$$\left(\text{XCO}_{2\text{gas/aq}}\right)_{\text{RM}} = \left(K_{\text{Hgas/aq}}^{\text{CC}}\right)_{\text{RM}} = \left(H(T)_{\text{gas/aq}}^{\text{1/cp}}\right)_{\text{RM}} * \frac{1}{R} * \frac{1}{T}.$$

At 298.15K , we find a 1.65% difference between XCO_2 obtained from $(\text{XCO}_2)_{\text{VH}}$ (1.202 gas/aq) and $(\text{XCO}_2)_{\text{RM}}$ (1.222 gas/aq).

Model selection results are provided Fig. 6 by comparing the aforementioned saturation indices with respect to calcite for a hypothetical geothermal solution. The calculations were performed under the conditions that may be observed in a direct-use application at the surface (1 atm or 0.1 MPa and 25°C). The hypothetical solution was charge-balanced to $\sim 0.1\%$ using Cl^- , and held at a constant pH of 5. Cl^- comprised 94% of the total anion budget and 94% of the TKS. This hypothetical solution most closely resembles a Type I Fluid (Table 1). The I.S. of each subsequent step was a doubling of the concentration of each dissolved species (eg. $2 * \text{I.S.}_{0.03} \approx \text{I.S.}_{0.06}$). The calculated Ω for each index along with the pH and TDS are provided in Supplementary Table 1. The $\log(\text{IAP}/K_{\text{sp}})$, SPI, and S_r saturation indices are each found using activities obtained from the Debye-Hückel (DH), Debye-Hückel-Extended (DH-E), Davies, and Bromley models.

To compare the effect of the two methods of obtaining XCO_2 , $I_{s\text{-VH}}$ corresponds to XCO_2 obtained from the Van't Hoff approach in Eq. (47), while $I_{s\text{-RM}}$ corresponds to XCO_2 obtained from the Rumpf and Mauer (1993) approach in Eq. (49). S_r -(Davies) estimates a much greater Ω than the other models Fig. 6A and B). This increase in Ω is because of the 0.3I term in Eq. (9). Conversely, many other models display a diminishing return effect, and the calculated Ω appears to show a logarithmic behavior proportional to I.S. (Fig. 6B). Interestingly, the Ω values obtained from $\log(\text{IAP}/K_{\text{sp}})$ -(DH), SPI-(DH), and S_r -(DH) all crest at I.S. between 0.12 and 0.48 mol/L before declining-indicating that the Debye-Hückel activity model is not recommended beyond these I.S. values. The SPI and LSI display little response in Ω at high I.S., which can be attributed to the 'smoothing out' by the logarithms used in their computation. There is little difference in the Ω between $I_{s\text{-VH}}$ and $I_{s\text{-RM}}$ (Supplementary Table 1), thus corroborating the calculations for XCO_2 in Eqs. (47) and (49), respectively. Moreover, $I_{s\text{-VH}}$ and $I_{s\text{-RM}}$ both estimate lower Ω than other models, possibly because alkalinity is assumed to be HCO_3^- (Oddo and Tomson, 1982; Corsi, 1986) and does not account for other species, such as CO_3^{2-} . If this ion is included, the numerator in the log term of Eq. (44) will increase along with Ω . If carbonate alkalinity (CA) is taken under consideration, then a common simplified form is provided (e.g. Andersen, 2002), as

$$\text{CA} = [\text{HCO}_3^-] + 2[\text{CO}_3^{2-}]. \quad (50)$$

An alternate form of CA can be found which incorporates both pH and pOH directly (Jensen, 2003; Michałowski and Asuero, 2012) via

$$\text{CA} = [\text{HCO}_3^-] + 2[\text{CO}_3^{2-}] + [\text{OH}^-] - [\text{H}^+]. \quad (51)$$

The resulting I_s values reported as I_{s1} and I_{s2} for Eqs. (50) and (51) for both $I_{s\text{-VH}}$ and $I_{s\text{-RM}}$, respectively, are greater than using $[\text{HCO}_3^-]$ for alkalinity alone (Fig. 6). The differences between both CA calculations are negligible (Supplementary Table 1 and Fig. 6) and at $\text{pH} 7$ become zero as Eq. (51) simplifies to Eq. (50). Andersen (2002) notes that for dilute surface waters ($\gamma = 1$ and total carbonate in the system is 0.005M) of circumneutral pH , HCO_3^- alone is satisfactory for alkalinity. Hedenquist (1990) also used HCO_3^- solely as alkalinity for geothermal waters with pH ranging from 4.7 to 5.9. This may provide a reasonable estimate since $[\text{CO}_3^{2-}]$ is negligible in this pH range (Bjerrum plot), and HCO_3^- is likely to be the main alkaline species (in the pH range of 4.7 to 5.9, $[\text{H}^+]$ would be > 2500 times greater than $[\text{OH}^-]$ at the median pH of 5.3). Nonetheless, because the TDS and pH values of geothermal fluids may be quite different from surficial waters, carbonate alkalinity obtained using Eq. (51) would most accurately model the true alkalinity of the fluid. As

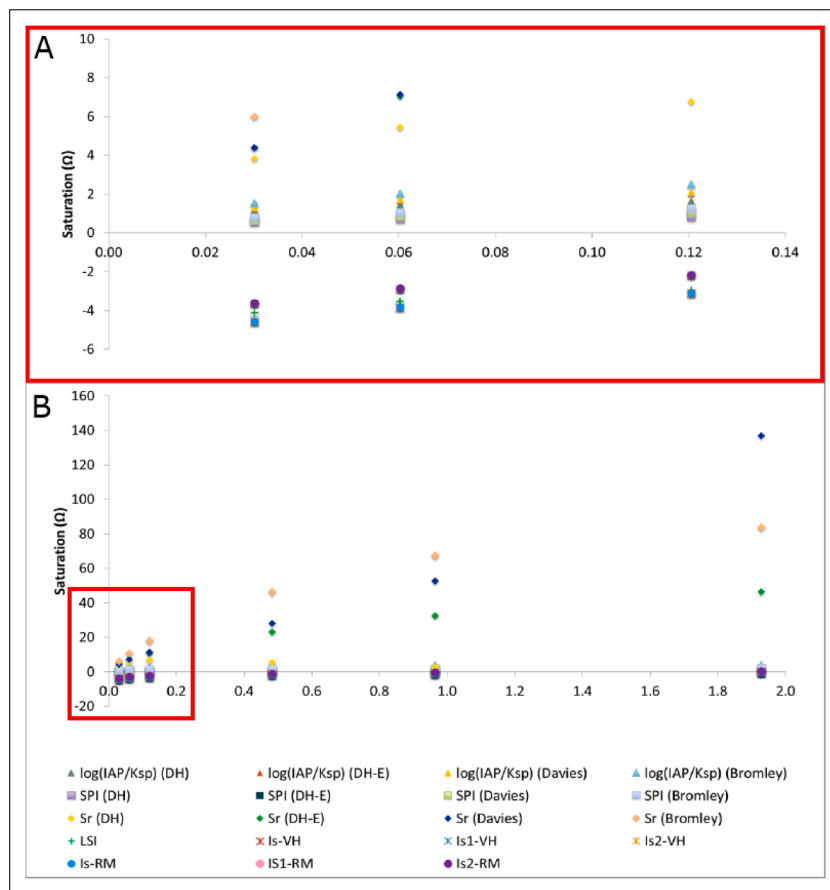


Fig. 6. Comparison of saturation indices and activity model calculations with respect to ionic strength for the mineral calcite. All Ω were determined for a hypothetical solution at 25 °C and 1 atm, and considered Al^{3+} , Ba^{2+} , Ca^{2+} , Cl^- , CO_3^{2-} , Fe^{2+} , H^+ , HCO_3^- , K^+ , Mg^{2+} , Na^+ , OH^- , Si^0 , and SO_4^{2-} ions. These data are provided in Supplementary Table 1. (A) $0.03 \text{ mol/L} < I < 0.12 \text{ mol/L}$. The large red rectangle indicates that this subframe is a zoomed-in segment of the whole I range. (B) $0.03 \text{ mol/L} < I < 1.93 \text{ mol/L}$. The small red square highlights the region in subframe A.

Fig. 6 and Supplementary Table 1 indicate, different saturation models yield different saturation values and can predict either supersaturation or undersaturation for the same fluid chemistry. Therefore, regardless of which saturation model is chosen, it is recommended to apply more than one to best model the expected variation in the fluid (Ungemach, 2003).

4.3. Scaling and treatment for geothermal systems

In the detailed example above highlighted calcite scaling, yet there are other minerals that commonly form scales- sulfides (Miller, 1980), other carbonates, silica (Barnes, 2015), and iron minerals (Li et al., 2020). These and other scale-forming minerals, their stability domain (pH, Eh), and treatment methods (such as the addition of anti-scaling agents, e.g., Bu et al. (2022)) for each are provided collectively in Table 2. Unfortunately, pH and Eh values for minerals (or solid phases) are sparse. Anion group stability, as found in Takeno (2005), is used to constrain the overall mineral stability. For example, phosphate (PO_4^{3-}) is the dominant species in the P-O-H system in water pH ranging from pH $> \sim 12$ and is not limited by Eh (vertical line on pH-Eh diagram)-it is stable in water (Takeno, 2005). This does not imply that if Ca^{2+} is present in hypothetical water at pH 13 and Eh 0 V, amorphous calcium phosphate will immediately precipitate. The fluid may or may not be supersaturated with respect to this solid phase. Rather, it only indicates that the speciations of the required ions necessary for precipitation are present-the ion concentrations (or activities) that may preclude precipitation. Despite this, anion pH-Eh stability diagrams are helpful. If the fluid in the amorphous calcium phosphate example above has a pH of 9 (still with Eh of 0 V) then the dominant species in the P-O-H systems is HPO_4^{2-} (Takeno, 2005). Now, the hypothetical water cannot precipitate amorphous calcium phosphate under these conditions because of the speciation of the polyatomic anion regardless of $[\text{Ca}^{2+}]$. Therefore,

scaling of this solid phase will not occur. Additionally, physical controls can be employed to prevent scaling. For example, scaling caused by mixing can be prevented by ensuring that water in the geothermal reservoir is above the level of the undesired water (Arnósson, 1992).

Scaling is an adverse problem encountered in geothermal systems, yet, if the geothermal fluid enters surficial runoff or is exposed to groundwater, it may be desirable to induce scaling (i.e., precipitation). Precipitations of solids from the geothermal fluid are necessary to prevent the downstream transport of toxic waste. For example, it is well known that arsenic is a toxic metal, and the dissolution of orpiment (As_2S_3) occurring in the geothermal reservoir produces either arsenious acid (H_3AsO_3) for low-sulfide waters (Eary, 1992), and $\text{H}_2\text{As}_3\text{S}_6$ for high-sulfide waters (Spycher and Reed, 1989; Eary, 1992). Therefore, precipitation of H_3AsO_3 may be enhanced or favored at lower pH and temperature. Similarly, if $\text{H}_2\text{As}_3\text{S}_6$ is present, a decrease in pH will reduce the solubility (Webster and Nordstrom, 2003).

5. Conclusions

Fluid-rock interactions are complex and highly variable systems that are subject to many variables. Two of these variables are pH and Eh and significantly control the dissolved ion concentration, the ion or molecule speciation, the rate of a reaction, and the direction or spontaneity of a reaction. Fig. 7 displays the interplay between these relationships with respect to pH and Eh, which are controlled by temperature and pressure.

Ultimately, for a dynamic system, even these master variables can change with respect to time-the only true parameter. Some considerations and suggestions for future work include:

- The relevance and importance of pH and Eh in predicting fluid-rock interactions cannot be overstated. While critical, these variables are

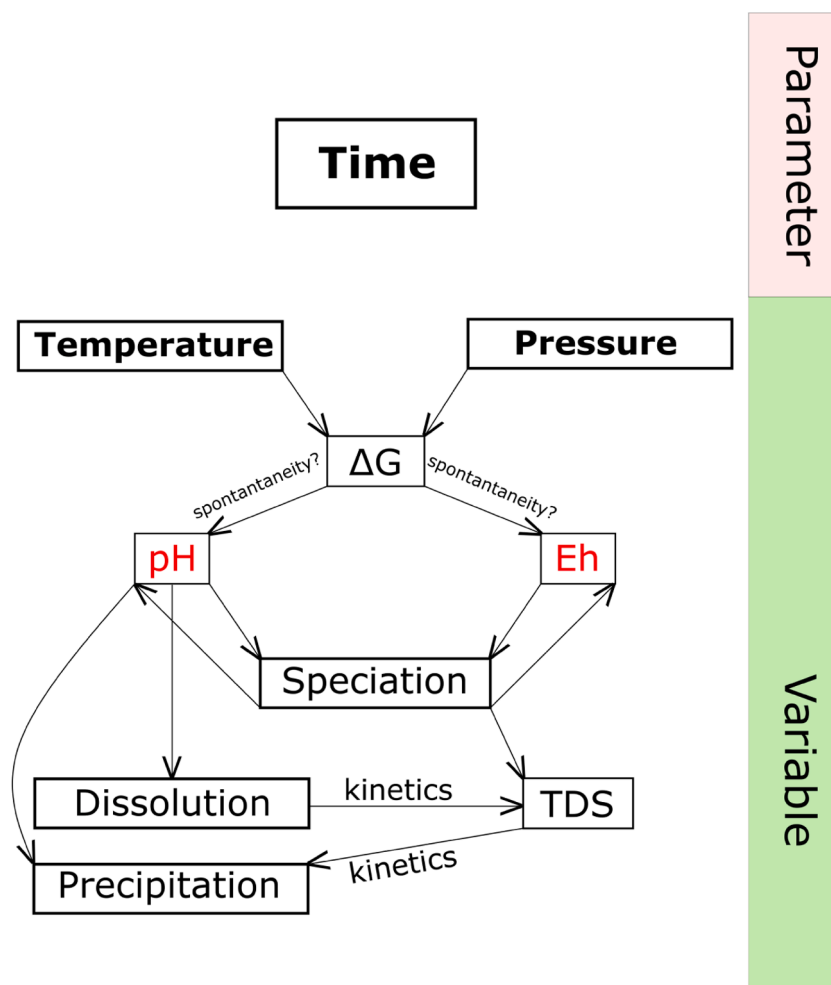


Fig. 7. Spider map illustrating the interplay and hierarchy between major variables and parameters that govern fluid-rock interaction.

closely related to and are dependent upon temperature and pressure, and it is impossible to explore pH and Eh without their consideration. Pressure and temperature (and composition) are related to the physical geothermal environment by reservoir depth (pressure), geothermal gradient (temperature), and reservoir HDR lithology (composition).

- Geothermal systems (particularly EGS, which may involve surface-level conditions) are highly complex. Geochemical models derived for one EGS site may not be suitable for another site even with similar characteristics. Reservoir evolution over time is another complicating factor (e.g., Bächler and Kohl, 2005; Scott and Driesner, 2018). Two of the most direct applications of these relationships to EGS are the mitigation of corrosion and scaling both in terms of maintaining an economically viable operation and ensuring the safety of the power plant. Corrosion can be reduced by an appropriate choice of material, as there are many grades of steel available. This decision should be made in accordance with the fluid chemistry, which reflects the fluid-rock interaction occurring within the EGS reservoir.
- Scaling can be addressed by manipulating the fluid composition (and physical controls of reservoir water level, e.g., Arnórsson (1992)). Chemical additives, or pH/Eh control, can alter the speciation of the ions in solution such that detrimental mineral scalants do not precipitate.
- The strength of a model depends in part on the quality of the initial data—a note made by many workers (e.g., Spycher and Reed, 1992). Future experiments could be made to improve thermodynamic data

on useful diagnostic minerals such as awaruite and heazlewoodite (McCullom and Bach, 2009) and solid solutions and dissolved species at high temperatures (Reed, 1982). Furthermore, extending the known behavior of activity model coefficient A to temperatures above 100 °C would improve activity coefficient calculations at temperatures encountered in geothermal settings. Also, there are polyatomic molecules such as H₂S and NH₃ (TKS molecules) that are not readily available in tables, thereby hindering activity and ionic strength calculations. Spycher and Reed (1989) state the need for additional experimentation to improve the stoichiometry of reactions involving arsenic and antimony sulfides at low temperatures. Results from such studies would have implications for mass balance and toxic waste generation from geothermal brines. Finally, even with excellent thermodynamic data, the data must be modeled appropriately and applied reasonably (Spycher and Reed, 1992; Nordstrom and Munoz, 1994).

Declaration of Competing Interest

The authors declare that they have no known competing financial interests or personal relationships that could have appeared to influence the work reported in this paper.

Data availability

We have shared all data in Tables and supplementary table

Acknowledgments

The authors' research and the time for compiling this review were supported by the Department of Energy Office of Energy Efficiency & Renewable Energy (DOE EERE) Geothermal Technologies Program Award # DE-EE0009597 to S. Sharma

Supplementary materials

Supplementary material associated with this article can be found, in the online version, at [doi:10.1016/j.geothermics.2023.102710](https://doi.org/10.1016/j.geothermics.2023.102710).

References

- Abas, N., Kalair, A., Khan, N., Kalair, A.R., 2017. Review of GHG emissions in Pakistan compared to SAARC countries. *Renew. Sustain. Energy Rev.* 80, 990–1016.
- Alt, J.C., Shanks III, W.C., 1998. Sulfur in serpentinized oceanic peridotites: serpentinization processes and microbial sulfate reduction. *J. Geophys. Res.* (103), 9917–9929.
- Arvanitis, A., Kavouri, K., Vougioukalakis, G., Karmis, P., Xenakis, M., Koufogiannis, I., Somataridou, V., Vakalopoulos, P., and Exioglou, D., 2020, Systematic and multidisciplinary exploration in the Lithotopos-Iraklia low enthalpy Geothermal field (Macedonia, Northern Greece), Proceedings World Geothermal Congress 2020 +1, April-October 2021, Reykjavik.
- Andersen, B.C., 2002. Understanding carbonate equilibria by measuring alkalinity in experimental and natural systems. *J. Geosci. Educ.* 50, 389–403.
- Anderson, A., Rezaei, B., 2019. Geothermal technology: trends and potential role in a sustainable future. *Appl. Energy* 248, 18–34.
- Andrews, J.E., Brimblecombe, P., Jickells, T.D., Liss, P.S., Reid, B.J., 2004. An Introduction to Environmental Chemistry. Blackwell Publishing, Oxford, p. 296.
- Andrews, J.N., Kay, R.L.F., 1983. The uranium and $^{234}\text{U}/^{238}\text{U}$ activity ratios of dissolved uranium in groundwaters from some Triassic sandstones in England. *Isot. Geosci.* 101–117.
- Antony, A., Low, J.H., Gray, S., Childress, A.E., Le-Clech, P., Leslie, G., 2011. Scale formation and control in high pressure membrane water treatment systems: a review. *J. Memb. Sci.* 383, 1–16.
- Ármansson, H., Kristmannsdóttir, H., 1992. Geothermal environmental impact. *Geothermics* 21, 869–880.
- Árnórsson, S., Sigurdsson, S., Svavarsson, H., 1982. The chemistry of geothermal waters in Iceland. I. Calculation of aqueous speciation from 0° to 370 °C. *Geochim. Cosmochim. Acta* 46, 1513–1532.
- Árnórsson, S., 1989. Deposition of calcium carbonate minerals from geothermal waters-theoretical considerations. *Geothermics* 18, 33–39.
- Árnórsson, S., 1992. Calcite deposition in geothermal wells caused by infiltrating seawater. In: Kharaka, Y.K., Maest, A.S. (Eds.), *Water-Rock Interaction, Volume 2: Moderate and High Temperature Environments*. A.A. Balkema, Rotterdam, Park City, Utah, pp. 1389–1392. Proceedings of the 7th International Symposium On Water-Rock Interaction.
- Arvanitis, A., Kavouri, K., Vougioukalakis, G., Karmis, P., Xenakis, M., Koufogiannis, I., Somataridou, V., Vakalopoulos, P., Exioglou, D., 2020. Systematic and multidisciplinary exploration in the lithotopos-iraklia low enthalpy geothermal field (Macedonia, Northern Greece). In: Proceedings of the World Geothermal Congress 2020 +1, April-October 2021, Reykjavik.
- ASTM, 2017. Standard Practice for Preparing, Cleaning, and Evaluating Corrosion test Specimens. ASTM International, West Conshohocken. G1-03 (Reapproved 2017)9.
- Bächler, D., Kohl, T., 2005. Coupled thermal-hydraulic-chemical modelling of enhanced geothermal systems. *Geophys. J. Int.* 161, 533–548.
- Baciu, F., Rusu-Casandra, A., Pastramă, S.F., 2020. Low strain rate testing of tensile properties of steel. *Mater. Today Proc.* 32, 128–132.
- Bahadori, A., Zendejboudi, S., Zahedi, G., 2013. A review of geothermal energy resources in Australia: current status and prospects. *Renew. Sustain. Energy Rev.* 21, 29–34.
- Bai, M., Reinicke, K.M., Teodoriu, C., Fichter, C., 2012. Investigation on water-rock interaction under geothermal hot dry rock conditions with a novel testing method. *J. Pet. Sci. Eng.* 90–91, 26–30.
- Bakker, R.J., 2012. Thermodynamic properties and applications of modified van-der-Waals equations of state. In: Morales-Rodríguez, R (Ed.), *Thermodynamics-Fundamentals and Its Application in Science*. InTech, pp. 163–190.
- Barnaby, R.J., Rimstidt, J.D., 1989. Redox conditions of calcite cementation interpreted from Mn and Fe contents of authigenic calcites. *Geol. Soc. Am. Bull.* 101, 795–804.
- Barnes, H.L., 2015. Hydrothermal processes. *Geochem. Perspect. Eur. Assoc. Geochem.* 4, 93.
- Bass-Becking, L.G.M., Kaplan, I.R., Moore, D., 1960. Limits of the natural environment in terms of pH and oxidation-reduction potentials. *J. Geol.* 68, 243–284.
- Beckers, K.F., Kolker, A., Pauling, H., McTigue, J.D., Kesseli, D., 2021. Evaluating the feasibility of geothermal deep direct-use in the United States. *Energy Convers. Manage.* 243, 114335.
- Bieling, V., Rumpf, B., Strepp, F., Mauer, G., 1989. An evolutionary optimization method for modeling the solubility of ammonia and carbon dioxide in aqueous solutions. *Fluid Ph. Equilib.* 53, 251–259.
- Bloomquist, R.G., 2003. Geothermal space heating. *Geothermics* 32, 513–526.
- Bragin, I.V., Kharitonova, N.A., Chelnokov, G.A., Aseeva, A.V., Chudaev, O.V., 2018. REY geochemistry in groundwater from Paratunka geothermal area (Kamchatka peninsula, Far East of Russia). *Environ. Earth Sci.* 77, 376.
- Bromley, L.A., 1973. Thermodynamic properties of strong electrolytes in aqueous solutions. *AIChE J.* 19, 313–320.
- Brookins, D.G., 1986. Geochemical behavior of antimony, arsenic, cadmium and thallium: Eh-pH diagrams for 25°C, 1-bar pressure. *Chem. Geol.* 54, 271–278.
- Brookins, D.G., 1988. Eh-pH Diagrams for Geochemistry. Springer-Verlag, Berlin, p. 176.
- Brown, K., 2011. Antimony and arsenic sulfide scaling in geothermal binary plants. In: Proceedings of the International Workshop on Mineral Scaling 2011, 25–27 May 2011, Manila.
- Bu, X., Jiang, K., Wang, X., Liu, X., Tan, X., Kong, Y., Wang, L., 2022. Analysis of calcium carbonate scaling and antiscaling field experiment. *Geothermics* 104, 102433.
- Cammarata, G., Cammarata, L., Petrone, G., 2014. Thermodynamic analysis of ORC for energy production from geothermal resources. *Energy Proc.* 45, 1337–1343.
- Cappetti, G., Ceppatelli, L., 2005. Geothermal power generation in Italy: 2000–2004 update report. In: Proceedings of the World Geothermal Congress 2005, 24–29 April 2005, Antalya.
- Carbonell, A.A., Pulido, R., DeLaune, R.D., Patrick Jr, W.H., 1999. Soluble barium in barite and phosphogypsum amended Mississippi River alluvial sediment. *J. Environ. Qual.* 28, 316–321.
- Carlin, J., 2004. Renewable energy in the United States. *Environ. Energy* 5, 347–363.
- Chang, L., Volpe, L., Wang, Y.L., Burke, M.G., Maurotto, A., Tice, D., Lozano-Perez, S., Scenini, F., 2019. Effect of machining on stress corrosion crack initiation in warm-forged type 304L stainless steel in high temperature water. *Acta Mater.* 165, 203–214.
- Chatterjee, R., Paul, S., Singha, D.K., Mukhopadhyay, M., 2015. Overpressure zones in relation to *in situ* stress for the Krishna-Godavari Basin, eastern continental margin of India: implications for hydrocarbon prospectively. In: Mukherjee, S (Ed.), *Petroleum Geosciences: Indian Contexts*. Springer, Cham, pp. 127–142.
- Chen, T., Wang, Q., Chang, F., 2016. CaCO₃ scale risk assessment-thermodynamics vs kinetics. In: Proceedings of the Corrosion 2016, NACE International, 7263, pp. 1–14. PaperDhahran.
- Chen, L.Q., 2019. Chemical potential and Gibbs free energy. *MRS Bull.* 44, 520–523.
- Chidambaram, S., Karmegam, U., Sasidhar, P., Prasanna, M.V., Manivannan, R., Arunachalam, S., Manikandan, S., Anandhan, P., 2011. Significance of saturation index of certain clay minerals in shallow coastal groundwater, in and around Kalpakkam, Tamil Nadu, India. *J. Earth Syst. Sci.* 120, 897–909.
- Chong, T.H., Sheikholeslami, R., 2001. Thermodynamics and kinetics for mixed calcium carbonate and calcium sulfate precipitation. *Chem. Eng. Sci.* 56, 5391–5400.
- Corsi, R., 1986. Scaling and corrosion in geothermal equipment: problems and preventive measures. *Geothermics* 15, 839–856.
- CRC Handbook of Chemistry and Physics, 2017. In: Haynes, W.M (Ed.), *Handbook of Chemistry and Physics 97th Edition 2016–2017*. Taylor & Francis, Boca Raton.
- Criaud, A., Fouillac, C., 1989. Sulfide scaling in low enthalpy geothermal environments: a survey. *Geothermics* 18, 73–81.
- Criaud, A., Fouillac, C., Marty, B., 1989. Low enthalpy geothermal fluids from the Paris Basin. 2-Oxidation-reduction state and consequences for the prediction of corrosion and sulfide scaling. *Geothermics* 18, 711–727.
- Crundwell, F.K., 2017. Path from reaction control to equilibrium constraint for dissolution reactions. *Am. Chem. Soc. Omega* 2, 4845–4858.
- Diamond, L.W., Alt-Epping, 2014. Predictive modeling of mineral scaling, corrosion and the performance of solute geothermometers in a granitoid-hosted, enhanced geothermal system. *Appl. Geochem.* 51, 216–228.
- DiPippo, R., 2015. Geothermal power plants: evolution and performance assessments. *Geothermics* 53, 291–307.
- Dissanayake, C.B., Jayasena, H.A.H., 1988. Origin of geothermal systems in Sri Lanka. *Geothermics* 17, 657–669.
- Dobson, P.F., Kneafsey, T.J., Nakagawa, S., Sonnenthal, E.L., Voltolini, M., Smith, J.T., Borglin, S.E., 2021. Fracture sustainability in enhanced geothermal systems: experimental and modelling constraints. *J. Energy Resour. Technol.* 143, 1–16.
- Eary, L.E., 1992. The Solubility of amorphous As₂S₃ from 25 to 90°C. *Geochim. Cosmochim. Acta* 56, 2267–2280.
- Ellis, A.J., 1979. Explored geothermal systems. In: Barnes, H. (Ed.), *Geochemistry of Hydrothermal Ore Deposits*, 2nd ed. Wiley-Interscience, New York City, pp. 632–683.
- Ellis Jr., P.F., Conover, M.F., 1981. *Materials Selection Guidelines For Geothermal Energy Utilization Systems*, Radian Corporation. Department of Energy, Austin, p. 696.
- Esteves, A.F., Santos, F.M., Magalhães Pires, J.C., 2019. Carbon dioxide as geothermal working fluid: an overview. *Renew. Sustain. Energy Rev.* 114, 109331.
- Faes, W., Lecompte, S., Van Bael, J., Salenbien, R., Bäßler, R., Bellemans, I., Cools, P., De Geyter, N., Morent, R., Verbeken, K., De Paep, M., 2019. Corrosion behavior of different steel types in artificial geothermal brines. *Geothermics* 82, 182–189.
- Fetter, C.W., 2001. *Applied Hydrogeology*, 4th ed. Pearson Education, Upper Saddle River, p. 597.
- EPRI, 1978. *Geothermal energy prospects for the next 50 years*, Electric Power Research Institute, Special Report ER-611-SR, February 1978, Palo Alto.
- Finster, M., Clark, C., Schroeder, J., Martino, L., 2015. Geothermal produced fluids: characteristics, treatment technologies, and management options. *Renew. Sustain. Energy Rev.* 50, 952–966.
- Fitts, C.R., 2002. *Groundwater Science*. Academic Press, San Diego, p. 451.
- Fournier, R.O., Thompson, J.M., Hutchinson, R.A., 1992. The geochemistry of hot spring waters at Norris Geyser Basin, Yellowstone National Park, USA. In: Kharaka, Y.K., Maest, A.S. (Eds.), *Water-Rock Interaction, Volume 2: Moderate and High Temperature Environments*, Proceedings of the 7th International Symposium On

- Water-Rock Interaction, WRI-7, 13-18 July 1992. Utah, A.A. Balkema, Rotterdam, Park City, pp. 1289–1292.
- Fridleifsson, I.B., 2001. Geothermal energy for the benefit of the people. *Renew. Sustain. Energy Rev.* 5, 299–312.
- Fridleifsson, I.B., Bertani, R., Lund, J.W., Rybach, L., 2008. The possible role and contribution of geothermal energy to the mitigation of climate change. O. Hohmeyer and T. Trittin (Eds.). In: *Proceedings of the IPCC Scoping Meeting on Renewable Energy Sources: 20–25 January 2008*. Lübeck.
- Frost, B.R., 1985. On the stability of sulfides, oxides, and native metals in serpentinite. *J. Petrol.* 26, 31–63.
- Furrer, G., Stumm, W., 1986. The coordination chemistry of weathering: I. Dissolution kinetics of δ - Al_2O_3 and BeO. *Geochim. Cosmochim. Acta* 50, 1847–1860.
- Gallup, D.L., 2011. pH modification scale control technology. In: *Proceedings of the International Workshop on Mineral Scaling 2011, 25–27 May 2011*, p. 39–46. Manila.
- Gallup, D.L., Featherstone, J.L., Reverente, J.P., Messer, P.H., 1995. Line mine: a process for mitigating injection well damage at the Salton Sea, California (USA) geothermal field. *Proc. World Geotherm. Congress 1995*, 2406–2414.
- Ganor, J., Mogollón, J.L., Lasaga, A.C., 1995. The effect of pH on kaolinite dissolution rates and on activation energy. *Geochim. Cosmochim. Acta* 59, 1037–1052.
- García, A.V., Thomsen, K., Tenby, E.H., 2006. Prediction of mineral scale formation in geothermal and oilfield operations using the Extended UNIQUAC model Part II. Carbonate-scaling minerals. *Geothermics* 35, 239–284.
- Garfias-Medias, L.F., Sykes, J.M., Tuck, C.D.S., 1996. The effect of phase compositions on the pitting corrosion of 25 Cr duplex stainless steel in chloride solutions. *Corros. Sci.* 38, 1319–1330.
- Garrels, R.M., Christ, C.L., 1965. Solutions, minerals, and equilibria. In: *Cronis, C. (Ed.), Harper's Geoscience Series*. Harper & Row, New York City, p. 450.
- Garrido Schneider, E.A., García-Gil, A., Vázquez-Suné, E., Sánchez-Navarro, J., 2016. Geochemical impacts of groundwater heat pump systems in an urban alluvial aquifer with evaporitic bedrock. *Sci. Total Environ.* 544, 354–368.
- Ghosh, T.K., 2011. Geothermal energy. In: *Ghosh, T.K., Prelas, M.A. (Eds.), Energy Resources and Systems V. 2: Renewable Resources*. Springer, Dordrecht, pp. 217–258.
- Giggenbach, W.F., 1977. The isotopic composition of sulfur in sedimentary rocks bordering the Taupo volcanic zone. In: *Ellis, A.J. (Ed.), Geochemistry 1977*. New Zealand Department of Scientific and Industrial Research Bulletin, pp. 57–64.
- Giggenbach, W.F., 1981. Geothermal mineral equilibria. *Geochim. Cosmochim. Acta* 45, 393–410.
- Giggenbach, W.F., 1984. Mass transfer in hydrothermal alteration systems—a conceptual approach. *Geochim. Cosmochim. Acta* 48, 2693–2711.
- Giggenbach, W.F., 1987. Redox processes governing the chemistry of fumarolic gas discharges from White Island, New Zealand. *Appl. Geochem.* (2), 143–161.
- Giggenbach, W.F., Glover, R.B., 1992. Tectonic regime and major processes governing the chemistry of water and gas discharges from the Rotorua Geothermal Field. *Geothermics* 21, 121–140.
- Given, R.K., Wilkinson, B.H., 1985. Kinetic control of morphology, composition, and mineralogy of abiogenic sedimentary carbonates. *J. Sediment. Petrol.* 55, 109–119.
- Gude, V.G., 2015. Energy storage for desalination processes powered by renewable energy and waste heat sources. *Appl. Energy* 137, 877–898.
- Gude, V.G., 2016. Geothermal source potential for water desalination—Current status and future perspective. *Renew. Sustain. Energy Rev.* 57, 1038–1065.
- Gunnlaugsson, E., 2012. Scaling in Geothermal Installation in Iceland. *United Nations University-Geothermal Training Programme and LaGeo*, 11–17 March 2012, Santa Tecla.
- Gunnlaugsson, E., Ármannsson, H., Thorhallsson, S., Steingrímsson, B., 2014. Problems in Geothermal Operation—Scaling and corrosion, Short Course VI On Utilization of Low-and Medium-Enthalpy Geothermal Resources and Financial Aspects of Utilization. *United Nations University-Geothermal Training Programme and LaGeo*, Santa Tecla, 23–29 March 2014.
- Hall, A.J., 1986. Pyrite-pyrrhotite redox reactions in nature. *Miner. Mag.* 50, 223–229.
- Hardardóttir, V., Oskarsson, F., 2017. Reykjanes Power Plant Steam and Water Quality in 2016, Technical Report Prepared for HS Orka, Project No.: 16-0011. Iceland Geosurvey, Reykjavík.
- Hedenquist, J.W., 1990. The thermal and geochemical structure of the Broadlands-Ohaaki geothermal system. *Geothermics* 19, 151–185.
- Hellmann, R., 1994. The albite-water system: Part I. The kinetics of dissolution as a function of pH at 100, 200, and 300°C. *Geochimica et Cosmochimica Acta* 58, 595–611.
- Hem, J.D., 1960. Some chemical relationships among sulfur species and dissolved ferrous iron. In: *Proceedings of the Geological Survey Water-Supply Paper 1459-C*, United States Department of The Interior, pp. 57–73.
- Henley, R.W., 1983. pH and silica scaling control in geothermal field development. *Geothermics* 12, 307–321.
- Henley, R.W., Brown, K.L., 1985. A practical guide to the thermodynamics of geothermal fluids and hydrothermal ore deposits. In: *Berger, B.R., Bethke, P.M. (Eds.), Geology and Geochemistry of Epithermal Systems V.2, Reviews in Economic Geology*. Society of Economic Geologists, pp. 25–44.
- Hofmann, H., Weides, S., Badadagli, T., Zimmermann, G., Moeck, I., Majorowicz, J., Unsworth, M., 2014. Potential for enhanced geothermal systems in Alberta, Canada. *Energy* 69, 578–591.
- D Holland, H., Malinin, S.D., 1979. The solubility and occurrence of non-ore minerals. In: *Barnes, H. (Ed.), Geochemistry of Hydrothermal Ore Deposits, 2nd ed.* Wiley-Interscience, New York City, pp. 461–508.
- Hua, Y., Yue, X., Liu, H., Zhao, Y., Wen, Z., Wang, Y., Zhang, T., Zhang, L., Sun, J., Neville, A., 2021. The evolution and characterization of the corrosion scales formed on 3Cr steel in CO_2 -containing conditions relevant to geothermal energy production. *Corros. Sci.* 183, 109342.
- Huang, H.H., 2016. The Eh-pH diagram and its advances. *Metals (Basel)* 6, 23.
- Huang, H.H., Cuentas, L., 1989. Construction of Eh-pH and other stability diagrams of uranium in a multicomponent system with a microcomputer-I. Domains of predominance diagrams. *Can. Metall. Q.* 28, 225–234.
- Jenkins, H.D.B., Thakur, K.P., 1979. Reappraisal of thermochemical radii for complex ions. *J. Chem. Educ.* 56, 576–577.
- Jensen, J.N., 2003. *A Problem-Solving Approach to Aquatic Chemistry*. Wiley, New York, p. 600.
- Kamila, Z., Kaya, E., Zarrouk, S.J., 2021. Reinjection in geothermal fields: an updated worldwide review 2020. *Geothermics* 89, 101970.
- Karlsdóttir, S.R., Csaki, I., Antoniac, I.V., Manea, C.A., Stefanoiu, R., Magnus, F., Miculescu, F., 2019. Corrosion behavior of AlCrFeNiMn high entropy alloy in a geothermal environment. *Geothermics* 81, 32–38.
- Kazemi, N., Samadi, F., 2016. Thermodynamic, economic and thermos-economic optimization of a new proposed organic Rankine cycle for energy production from geothermal resources. *Energy Convers. Manage.* 121, 391–401.
- Kruszewski, M., Hofmann, H., Gomez-Alvarez, F., Bianco, C., Jimenez-Haro, A., Garduño, H., Liotta, D., Trumpy, E., Brogi, A., Wheeler, W., Bastesen, E., Parisio, F., Saenger, E.H., 2021. Integrated stress field estimation and implications for enhanced geothermal system development in Acoculco, Mexico. *Geothermics* 89, 101931.
- Lahan, M.M., Villafuerte, G., Stevens, L., 2020. Geothermal energy resources of Papua New Guinea: country update. In: *Proceedings of the World Geothermal Congress 2020+1, April-October 2021*. Reykjavik.
- Lammers, K., Smith, M.M., Carroll, S.A., 2017. Muscovite dissolution kinetics as a function of pH at elevated temperature. *Chem. Geol.* 466, 149–158.
- Langelier, W.F., 1936. The analytical control of anti-corrosion water treatment. *J. Am. Water Works Assoc.* 28, 1500–1521.
- Lasaga, A.C., Soler, J.M., Ganor, J., Burch, T.E., Nagy, K.L., 1994. Chemical weathering rate laws and global geochemical cycles. *Geochim. Cosmochim. Acta* 58, 2361–2386.
- Lee, B.I., Kesler, M.G., 1975. A generalized thermodynamic correlation based on three-parameter corresponding states. *AIChE J.* 21, 510–527.
- Li, Y., Pang, Z., Galeczka, I.M., 2020. Quantitative assessment of calcite scaling of a high temperature geothermal well in the Kangding geothermal field of Eastern Himalayan Syntax. *Geothermics* 87, 101844.
- Liu, W., Meinel, D., Weiland, C., Spliethoff, H., 2014. Investigation of hydrofluoroolefins as potential working fluids in organic Rankine cycle for geothermal power generation. *Energy* 67, 106–116.
- Loredo, C., Ordóñez, A., García-Ordiales, E., Álvarez, R., Roqueñi, N., Cienfuegos, P., 2017. Hydrochemical characterization of a miner water geothermal energy resource in NW Spain. *Sci. Total Environ.* 576, 59–69.
- Lund, J.W., 1997. Direct heat utilization of geothermal resources. *Renewable Energy* 10, 403–408.
- Macdonald, D.D., 1980. Thermodynamics of corrosion for geothermal systems. In: *Casper, L.A., Pinchback, T.R. (Eds.), Geothermal Scaling and Corrosion*. ASTM, pp. 10–23. STP-717.
- Machel, H.G., 2001. Bacterial and thermochemical sulfate reduction in diagenetic settings—old and new insights. *Sediment. Geol.* 140, 143–175.
- Majorowicz, J., Grasby, S.E., 2010. High potential regions for enhanced geothermal systems in Canada. *Nat. Resour. Res.* 19, 177–188.
- Majorowicz, J., Weides, S., 2012. Is it feasible to use engineered geothermal systems to produce electrical energy in Alberta Basin? *CanGRC Rev.* i.3, 2–3.
- Manov, G.G., Bates, R.G., Hamer, W.J., Acree, S.F., 1943. Values of the constants in the Debye-Hückel Equation for activity coefficients. *Contrib. Natl. Bur. Stand.* 65, 1765–1767.
- Marion, G.M., 2001. Carbonate mineral solubility at low temperatures in the Na-K-Mg-Ca-H-Cl-SO₄-OH-HCO₃-CO₃-CO₂-H₂O system. *Geochim. Cosmochim. Acta* 65, 1883–1896.
- McCullom, T.M., Bach, W., 2009. Thermodynamic constraints on hydrogen generation during serpentinization of ultramafic rocks. *Geochim. Cosmochim. Acta* 73, 856–875.
- McQuarrie, D.A., Simon, J.D., 1997. *Physical Chemistry: A Molecular Approach*. University Science Books, Sausalito, p. 1360.
- Michałowski, T., Asuero, A.G., 2012. New approaches in modeling carbonate alkalinity and total alkalinity. *Crit. Rev. Anal. Chem.* 42, 220–244.
- Miller, R.L., 1980. Chemistry and materials in geothermal systems. In: *Casper, L.A., Pinchback, T.R. (Eds.), Geothermal Scaling and Corrosion, ASTM STP 717*. American Society for Testing and Materials, Philadelphia, pp. 3–9.
- Mock, J.E., Tester, J.W., Wright, M.P., 1997. Geothermal energy from the Earth: its potential impact as an environmentally sustainable resource. *Ann. Rev. Energy Environ.* 22, 305–356.
- Moeck, I.S., 2014. Catalog of geothermal play types based on geologic controls. *Renew. Sustain. Energy Rev.* 37, 867–882.
- Monnin, C., 1994. Density calculation and concentration scale conversions for natural waters. *Comput. Geosci.* 20, 1435–1445.
- Mundhenk, N., Knauss, K.G., Bandaru, S.R.S., Wonneberger, R., Devine, T.M., 2019. Corrosion of carbon steel and the passivating properties of films formed under high-PT geothermal conditions. *Sci. Total Environ.* 677, 307–314.
- Ngothai, Y., Lane, D., Kuncoro, G., Yanagisawa, N., Rose, P., Pring, A., 2012. Effect of geothermal brine properties on silica scaling in enhanced geothermal systems. *Geotherm. Resour. Council Trans.* 26, 871–880.
- Nogara, J., Zarrouk, S.J., 2018a. Corrosion in geothermal environment: part 1: fluids and their impact. *Renew. Sustain. Energy Rev.* 82, 1333–1346.
- Nogara, J., Zarrouk, S.J., 2018b. Corrosion in geothermal environment Part 2: metals and alloys. *Renew. Sustain. Energy Rev.* 82, 1347–1363.

- Nordstrom, D.K., Munoz, J.L., 1994. *Geochemical Thermodynamics*, 2nd ed. Blackwell Scientific Publications, Boston, p. 493.
- Nikitasari, A., Prasetyo, M.A., Riastuti, R., Mabruhi, E., 2019. Pitting corrosion resistance of CA6NM as geothermal turbine blade material in simulated artificial geothermal brine. In: *Proceedings of the IOP Conference Series: Materials Science and Engineering*, 541, 012016.
- Oddo, J.E., Tomson, M.B., 1982. Simplified calculations of CaCO₃ saturation at high temperatures and pressures in brine solutions. *J. Petrol. Technol.* (7), 1583–1590.
- Olasolo, P., Juárez, M.C., Morales, M.P., D'Amico, S., Liarte, I.A., 2016. Enhanced geothermal systems (EGS): a review. *Renew. Sustain. Energy Rev.* 56, 133–144.
- Filmtec, D., n.d. *FILMTEC Reverse Osmosis Membranes: Technical Manual*, Dow Water & Process Solutions, Form No. 609-00071-0416, Dow Chemical Company, pp. 181. 2023.
- Palandri, J.L., and Kharaka, Y.K., 2004. A compilation of rate parameters of water-mineral interaction kinetics for application to geochemical modeling, US Geological Survey Open File Report 2004-1068, pp. 64.
- Parkhurst, D.L., Appelo, C.A.J., 2013. Description of input and examples for PHREEQCVersion 3—a computer program for speciation, batch-reaction, one-dimensional transport, and inverse geochemical calculations. U.S. Geological Survey Techniques and Methods, p. 497. Book 6-A43.
- Pátzay, G., Stáhl, G., Kármán, F.H., Kálmán, E., 1998. Modeling of scale formation and corrosion from geothermal water. *Electrochim. Acta* 43, 137–147.
- Peng, D.Y., Robinson, D.B., 1976. A new two-constant equation of state. *Ind. Eng. Chem. Fundam.* 15, 59–64.
- Perkins, E., 2003. *Fundamental Geochemical Processes Between CO₂, Water and Minerals*. Alberta Innovates-Technology Futures, Edmonton, p. 9.
- Petro, M., Zesch, J., Chang, N., Bell, A., Kole, A., Rodkin, A., Dobson, P.F., Jung, Y., Xu, T., 2013. Experimental study of rock-fluid interactions using automated multi-channel system operated under conditions of CO₂-based geothermal systems. In: *Proceedings of the 38th Workshop on Geothermal Reservoir Engineering*, Stanford University, SGP-TR-198, 11-13 February 2013, Stanford.
- Phillips, S.L., Mathur, A.K., Doebler, R.E., 1977. A survey of treatment methods for geothermal fluids. In: *Proceedings of the SPE International Oilfield and Geothermal Chemistry Symposium*, SPE-6606-MS, 27-28 June 1977. La Jolla.
- Pitzer, K.S., 1973. Thermodynamics of electrolytes. I. Theoretical basis and general equations. *J. Phys. Chem.* 77, 268–277.
- Pitzer, K.S., Mayorga, G., 1973. Thermodynamics of electrolytes. II. Activity and osmotic coefficients for strong electrolytes with one or both ions univalent. *J. Phys. Chem.* 77, 2300–2308.
- Plummer, L.N., Parkhurst, D.L., Fleming, G.Q., and Dunkle, S.A., 1988. A computer program incorporating Pitzer's equations for calculation of geochemical reactions in brines. U.S. Geological Survey, Water-Resources Investigations Report 88-4153, pp. 309.
- Pope, J.G., McConchie, D.M., Clark, M.D., Brown, K.L., 2004. Diurnal variations in the chemistry of geothermal fluids after discharge. *Champagne Pool, Waitapu, N. Z. Chem. Geol.* 203, 253–272.
- Pourbaix, M., 1949. Corrosion, passivity and passivation from the thermodynamic point of view. *Corrosion* 121–133.
- Pourbaix, M., 1950. Some applications of electrochemical thermodynamics. *Corrosion* 6, 395–404.
- Pourbaix, M., 1974. Applications of electrochemistry in corrosion science and in practice. *Corros. Sci.* 14, 25–82.
- Qi, W., Gao, Q., Zhao, Y., Zhang, T., Wang, F., 2021. Insight into the stress corrosion cracking of HP-13Cr stainless steel in the aggressive geothermal environment. *Corros. Sci.* 190, 109699.
- Rafferty, K., 1999. *Scaling in Geothermal Heat Pump systems*, Oregon Institute of Technology, and Idaho Operations Office. US Department of Energy, Idaho Falls.
- Reed, M.H., 1982. Calculation of multicomponent chemical equilibria and reaction processes in systems involving minerals, gases and an aqueous phase. *Geochim. Cosmochim. Acta* 46, 513–528.
- Redlich, O., Kwong, J.N.S., 1949. On the thermodynamic solutions. V. An equation of state. Fugacities of gaseous solutions. *Chem. Rev.* 44, 233–244.
- Regenspurg, S., Wiersberg, T., Brandt, W., Huenges, E., Saadat, A., Schmidt, K., Zimmermann, G., 2010. Geochemical properties of saline geothermal fluids from the *in-situ* geothermal laboratory Groß Schönebeck (Germany). *Geochemistry* 70, 3–12.
- Rodríguez, C.E.C., Palacio, J.C.E., Venturini, O.J., Lora, E.E.S., Cobas, V.M., Marques dos Santos, D., Dotto, F.R.L., Gialluca, V., 2013. Exergetic and economic comparison of ORC and Kalina cycle for low temperature enhanced geothermal system in Brazil. *Appl. Therm. Eng.* 52, 109–119.
- Roedder, E., 1979. Fluid inclusions as samples of ore fluid. In: Barnes, H. (Ed.), *Geochemistry of Hydrothermal Ore Deposits*, 2nd ed. Wiley-Interscience, New York City, pp. 684–737.
- Rojas-Hernández, A., Ramírez, M.T., Ibáñez, J.G., González, I., 1991. Construction of multicomponent Pourbaix diagrams using generalized species. *J. Electrochem. Soc.* 138, 365–371.
- Rowan, E.L., Engle, M.A., Kirby, C.S., Kraemer, T.F., 2011. Radium Content of oil-and Gas-Field Produced Waters in the Northern Appalachian Basin (USA): Summary and Discussion of Data. US Geological Survey, Department of the Interior, Reston, p. 38. *Scientific Investigations Report 2011-5135*.
- Rumpf, B., Maurer, G., 1993. An experimental and theoretical investigation on the solubility of carbon dioxide in aqueous solutions of strong electrolytes. *Ber. Bunsenges. Phys. Chem.* 97, 85–97.
- Sander, R., 2015. *Compilation of Henry's law constants (version 4.0) for water as solvent*. *Atmos. Chem. Phys.* 15, 4399–4981.
- Scheiber, J., Nitschke, F., Seibt, A., Genter, A., 2012. Geochemical and mineralogical monitoring of the geothermal power plant in Soultz-Sous-Forêts (France). In: *Proceedings of the 37th Workshop on Geothermal Reservoir Engineering*, Stanford University, SGP-TR-194, 30 January-1 February 2012, Stanford.
- Schütz, F., Winterleitner, G., Huenges, E., 2018. Geothermal exploration in a sedimentary basin: new continuous temperature data and physical rock properties from northern Oman. *Geotherm. Energy* 6, 1–23.
- Scott, S.W., Driesner, T., 2018. Permeability changes resulting from quartz precipitation and dissolution around upper crustal intrusions. *Geofluids* 2018, 6957306.
- Setiawan, F.A., Rahayuningsih, E., Petrus, H.T.B.M., Nurpratama, M.I., Perdana, I., 2019. Kinetics of silica precipitation in geothermal brine with seeds addition: minimizing silica scaling in a cold-reinjection system. *Geotherm. Energy* (7), 1–16.
- Seyfried Jr, W.E., Mottl, M.J., 1982. Hydrothermal alteration of basalt by seawater under seawater-dominated conditions. *Geochim. Cosmochim. Acta* 46, 985–1002.
- Sharma, S., Agrawal, V., McGrath, S., Hakala, A.J., Lopano, C., Goodman, A., 2021. Geochemical controls on CO₂ interactions with deep subsurface shales: implications for geologic carbon sequestration, environmental science: processes impacts. *R. Soc. Chem.* 23, 1278–1300.
- Shaver, R.B., 1993. Field vs. lab alkalinity and pH: effects on ion balance and calcite saturation index. *Ground. Monit. Remed.* 13, 104–112.
- Sheikholeslami, R., 2005. Scaling potential index (SPI) for CaCO₃ based on Gibbs free energies. *AlChE J.* 51, 1782–1789.
- Sim, L.N., Chong, T.H., Taheri, A.H., Sim, S.T.V., Lai, L., Krantz, W.B., Fane, A.G., 2018. A review of fouling indices and monitoring techniques for reverse osmosis. *Desalination* 434, 169–188.
- Simmons, S.F., Christenson, B.W., 1994. Origins of calcite in a boiling geothermal system. *Am. J. Sci.* 294, 361–400.
- Slater, J.C., 1964. Atomic radii in crystals. *J. Chem. Phys.* 41, 3199–3204.
- Smith, R., Inomata, H., Peters, C., 2013. *Introduction to Supercritical Fluids: A spreadsheet-Based Approach*, 4th ed. Elsevier, Amsterdam, p. 729.
- Söhnel, O., Garside, J., 1992. *Precipitation: Basic Principles and Industrial Applications*. Butterworth-Heinemann, Oxford, p. 391.
- Spycher, N.F., Reed, M.H., 1989. As(II) and Sb(III) sulfide complexes: an evaluation of stoichiometry and stability from existing experimental data. *Geochim. Cosmochim. Acta* 53, 2185–2194.
- Spycher, N.F., Reed, M.H., 1992. Microcomputer-based modeling of speciation and water-mineral-gas reactions using programs SOLVEQ and CHILLER. In: Kharaka, Y. K., Maest, A.S. (Eds.), *Water-Rock Interaction, Volume 2: Moderate and High Temperature Environments*. A.A. Balkema, Rotterdam, Park City, Utah, pp. 1087–1090. *Proceedings of the 7th International Symposium On Water-Rock Interaction*.
- Stáhl, G., Pátzay, G., Weiser, L., Kálmán, E., 2000. Study of calcite scaling and corrosion processes in geothermal systems. *Geothermics* 29, 105–119.
- Stefánsson, A., Arnórsson, S., 2002. Gas pressures and redox reactions in geothermal fluids in Iceland. *Chemical Geology* 190, 251–271.
- Stefánsson, A., Gíslason, S.R., 2001. Chemical weathering of basalts, southwest Iceland: effect of rock crystallinity and secondary minerals on chemical fluxes to the ocean. *Am. J. Sci.* 301, 513–556.
- Stefánsson, V., 2005. World geothermal assessment. In: *Proceedings of the World Geothermal Congress 2005, 24–29 April 2005*. Antalya.
- Stoljarova, A., Regenspurg, S., Bäßler, R., Mathiesen, T., Nielsen, J.B., 2021. Effect of lead and copper containing brine on steel materials for geothermal applications—a corrosion study. *Geothermics* 91, 102024.
- Stutz, G.R., Shope, E., Aguirre, G.A., Batir, J., Frone, Z., Williams, M., Reber, T.J., Wheelton, C.A., Smith, J.D., Richards, M.C., Blackwell, D.D., Tester, J.W., Stedinger, J.R., Jordan, T.E., 2015. Geothermal energy characterization in the Appalachian Basin of New York and Pennsylvania. *Geosphere* 11, 1291–1304.
- Suganthi, L., Samuel, A.A., 2012. Energy models for demand forecasting—a review. *Renew. Sustain. Energy Rev.* 16, 1223–1240.
- Takeno, N., 2005. *Atlas of Eh-pH Diagrams Intercomparison of Thermodynamic Databases*. National Institute of Advanced Industrial Science and Technology, Research Center for Deep Geological Environments, p. 288. *Geological Survey of Japan Open File Report No. 419*.
- Tester, J.W., Anderson, B.J., Batchelor, A.S., Blackwell, D.D., DiPippo, R., Drake, E.M., Garnish, J., Livesay, B., Moore, M.C., Nichols, K., Petty, S., Toksöz, M.N., Veatch Jr., R.W., 2006. *The Future of Geothermal Energy: Impact of Enhanced Geothermal Systems (EGS) On the United States in the 21st Century*. Massachusetts Institute of Technology, and Idaho National Laboratory, US Department of Energy, Idaho Falls.
- Tester, J.W., Holgate, H.R., Armellini, F.J., Webley, P.A., Killilea, W.R., Hong, G.T., Barner, H.E., 1993. Supercritical water oxidation technology: a review of process development and fundamental research. In: Tedder, D.W., Pohland, F.G. (Eds.), *Emerging Technologies in Hazardous Waste Management III*, ACS Symposium Series. American Chemical Society, Washington.
- Tulloch, A.J., 1982. *Mineralogical observations on carbonate scaling in geothermal wells at Kawerau and Broadlands, N.Z.* *Proceedings 4th New Zealand Geothermal Workshop, October 1982, Auckland*, p. 131–134.
- Ungemach, P., 2003. Reinjection of cooled geothermal brines into sandstone reservoirs. *Geothermics* 32, 743–761.
- Utami, W.S., Herdianita, N.R., Atmaja, R.W., 2014. The effect of temperature and pH on the formation of silica scaling of the Dieng Geothermal Field, Central Java, Indonesia. In: *Proceedings of the 39th Workshop on Geothermal Reservoir Engineering*, Stanford University, SGP-TR-202, 24-26 February 2014, Stanford.
- van de Lisdonk, C.A.C., Rietman, B.M., Heijman, S.G.J., Sterk, G.R., Schippers, J.C., 2001. Prediction of supersaturation and monitoring of scaling in reverse osmosis and nanofiltration membrane systems. *Desalination* 138, 259–270.

- van der Meer, F., Hecker, C., van Ruitenbeek, F., van der Werff, H., de Wijkerslooth, C., Wechsler, C., 2014. Geologic remot sensing for geothermal exploration: a review. *Int. J. Appl. Earth Obs. Geoinf.* 33, 255–269.
- van der Waals, J.D., 1873. *Over De Continuïteit van Den Gas-en Vloeïstoftoestand*, PhD Dissertation. University of Leiden, Leiden, p. 134.
- Varga, A., Bozsó, G., Garaguly, I., Raucsik, B., Bencsik, A., Kóbor, B., 2019. Cements, waters, and scales: an integrated study of the Szeged Geothermal Systems (SE Hungary) to characterize natural environmental conditions of the thermal aquifer. *Geofluids* 2019, 1–21.
- Verink Jr., E.D., 2000. Simplified procedure for constructing Pourbaix diagrams. In: Revie, RW (Ed.), *Uhlig's Corrosion Handbook*, 2nd ed. Wiley, New York City, pp. 111–124.
- von Jouanne, A., Brekken, T.K.A., 2017. Ocean and geothermal energy systems. *IEEE Proc. IEEE* 105, 2147–2165.
- Webster, J.G., Nordstrom, D.K., 2003. Geothermal arsenic: the source, transport and fate of arsenic in geothermal systems. In: Welch, A.H., Stollenwerk, K.G. (Eds.), *Arsenic in Groundwater: Geochemistry and Occurrence*. Kluwer Academic Publishers, New York City, pp. 101–127.
- Wheeland, K.G., Robertson, R., 1987. Lime scaling at wastewater treatment facilities in the Noranda Group, Crystallization and Precipitation. In: *Proceedings of the International Symposium*, p. 249-257, 5-7 October 1987. Saskatoon.
- Williams, A.E., McKibben, M.A., 1989. A brine interface in the Salton Sea Geothermal System, California: fluid geochemical and isotopic characteristics. *Geochim. Cosmochim. Acta* 53, 1905–1920.
- Williams, B.G., Patrick Jr., W.H., 1977. A computer method for the construction of Eh-pH diagrams. *J. Chem. Educ.* 54, 107.
- Wilson, T.P., Long, D.T., 1993. Geochemistry and isotope chemistry of Ca-Na-Cl brines in Silurian strata, Michigan Basin, U.S.A. *Appl. Geochem.* 8, 507–524.
- Wu, Y., Li, P., 2020. The potential of coupled carbon storage and geothermal extraction in a CO₂-enhanced geothermal system: a review. *Geotherm. Energy* 19.
- Yanagisawa, N., Masuda, Y., Asanuma, H., Osato, K., Sakura, K., 2021. Estimation of casing material corrosion rates for supercritical geothermal development. *Geothermics* 96, 102149.
- Yunker, L.W., Kasameyer, P.W., Tewhey, J.D., 1982. Geological, geophysical, and thermal characteristics of the Salton Sea Geothermal Field, California. *J. Volcanol. Geother. Res.* 12, 221–258.
- Yue, X., Zhang, L., Ma, L., Lu, M., Neville, A., Hua, Y., 2021. Influence of a small velocity variation on the evolution of the corrosion products and corrosion behaviour of super 13Cr SS in a geothermal CO₂ containing environment. *Corros. Sci.* 178, 108983.
- Zhang, J., Laboureur, D., Liu, Y., Mannan, M.S., 2016. Lessons learned from a supercritical pressure BLEVE in Nihon Dempa Kogyo Crystal Inc. *J. Loss Prev. Process Ind.* 41, 315–322.
- Zhang, Y., Wu, S., Cheng, F., 2022. A duplex stainless steel (DSS) with striking tensile strength and corrosion resistance through wire arc-additive manufacturing (WAAM) using a newly developed flux-cored wire. *Mater. Lett.* 313, 131760.
- Zolfaghroshan, M., Khamehchi, E., 2020. A rigorous approach to scale formation and deposition modelling in geothermal wellbores. *Geothermics* 87, 101841.
- Zotzmann, J., Regenspurg, S., 2015. Evaluating the efficiency of scaling inhibitors in geothermal fluids at high pressures and high temperatures. In: *Proceedings of the World Geothermal Congress 2015*, 19–25 April 2015. Melbourne.